Timing and controls on Ni-Cu-PGE mineralization within the Crystal Lake Intrusion, 1.1 Ga Midcontinent Rift

J.W. Smith[1]*, W. Bleeker[1], M. Hamilton[2], D. Petts[1], S.L. Kamo[2], and D. Rossell[3]

[1]Geological Survey of Canada, 601 Booth Street, Ottawa, Ontario K1A 0E8
[2]Jack Satterly Geochronology Laboratory, University of Toronto, 22 Russell Street, Toronto, Ontario M5S 3B1
[3]Rio Tinto Exploration Canada Inc., 1300 Walsh Street, Thunder Bay, Ontario P7E 4X4
*Corresponding author's e-mail: jennifer.smith6@canada.ca

ABSTRACT

North America's 1.1 Ga Midcontinent Rift (MCR) hosts a diverse range of ultramafic and mafic intrusions, many of which contain Ni-Cu-PGE mineralization. The gabbroic, sulphide-bearing Crystal Lake Intrusion was emplaced between 1095–1091 Ma during the 'main-stage' of rift evolution. The Ni-Cu-PGE mineralization shows a close spatial association with contaminated, Cr-spinel-bearing, vari-textured gabbros. Despite the MCR having a rich legacy of research, the temporal and spatial controls on ore formation, in addition to the processes critical for ore genesis, remain poorly constrained. Here we present new field, petrographic, and mineralogical observations, with preliminary U-Pb zircon and baddeleyite isotope dilution-thermal ionization mass spectrometry (ID-TIMS) results for various phases of the Crystal Lake Intrusion to resolve questions regarding the timing of emplacement and its relationship to other MCR magmatic events, such as the Mount Mollie dyke, the Pigeon River dykes, and the Cu-Ni-bearing Duluth Complex.

Results suggest that the sulphide ores at Crystal Lake were formed under low confining pressures from a magma saturated in volatiles through contamination. The addition of crustal S prior to emplacement, by assimilation and melting of wall rocks and xenoliths entrained in the magma, is considered critical for the genesis of the ores. The local addition of S in situ, as indicated by S/Se ratios, likely contributed only minor S into the system and is not considered essential for S saturation. Reworking of the magmatic system is indicated within the taxitic units by local brecciation, 'ripped' sulphide clasts and large (>1 cm) globular sulphides, which may indicate minimal transportation of the ores and the potential of a deeper sulphide pool/source. The pronounced magnetic anomaly of the southern limb may suggest the presence of a feeder dyke in the south.

Palladium (91–99%) and Pt (>99%) reside primarily as platinum group minerals (PGMs) in association with sulphides. The PGM assemblage, which is largely controlled by the availability of semi-metals through contamination, is dominated by Pt arsenides, Pd-Bi-Sb±Te phases, Pd-Sn±Sb phases, Pd bismuthides, and Pd antimonides. The similarity of the PGM assemblage throughout the Crystal Lake Intrusion indicates crystallization from compositionally similar magmas. The distribution of elements is consistent with the fractionation of a sulphide liquid, with later low-temperature alteration locally remobilizing elements at the micro-scale. The preferential partitioning of Mo, As, Bi, Re, and Pd into discrete parallel linear features and the development of a micro-fabric within unaltered sulphide globules suggests localized remobilization of select elements post-sulphide fractionation.

INTRODUCTION

North America's Midcontinent Rift (MCR) represents one of the best preserved intra-continental rift systems of the late Mesoproterozoic (Wold and Hinze, 1982; Green, 1983; Van Schmus and Hinze, 1985; Hutchinson et al., 1990; Miller and Nicholson, 2013). The ca. 1.1 Ga 'failed rift' system hosts a range of mafic-ultramafic, carbonatitic and alkaline intrusions (*see* compilation in Bleeker et al., 2020), many of which are actively being explored for a range of commodities (e.g. Ni, Cu, PGE, Co, Cr, V, Ti, Fe, Nb). The magmatic Ni-Cu-PGE sulphide deposits occur in association with a variety of mafic and mafic-ultramafic intrusions. Like many other world-class Ni-Cu deposits (e.g. Norilsk, Voisey's Bay, Raglan), this mineralization shows a close spatial and temporal relationship with large volumes of magma erupted at or near the margins of Archean cratons and/or in association with trans-lithospheric faults (e.g. Naldrett, 1997; Begg et al., 2010; Lightfoot and Evans-Lamswood, 2015, and references therein).

The MCR mafic and mafic-ultramafic intrusions that host Ni-Cu-PGE mineralization not only show considerable variability in their size, shape, and internal igneous stratigraphy but also in their style of mineralization (*see* Bleeker et al., 2020 and references

Smith, J.W., Bleeker, W., Hamilton, M., Petts, D., Kamo, S.L., and Rossell, D., 2020. Timing and controls in Ni-Cu-PGE mineralization within the Crystal Lake Intrusion, 1.1 Ga Midcontinent Rift; *in* Targeted Geoscience Initiative 5: Advances in the understanding of Canadian Ni-Cu-PGE and Cr ore systems – Examples from the Midcontinent Rift, the Circum-Superior Belt, the Archean Superior Province, and Cordilleran Alaskan-type intrusions, (ed.) W. Bleeker and M.G. Houlé; Geological Survey of Canada, Open File 8722, p. 37–63. https://doi.org/10.4095/326881

therein). The Ni-Cu-PGE sulphide mineralization within the MCR can be broadly classified into four types: 1) disseminated sulphide mineralization associated with gabbroic to troctolitic intrusions (e.g. Duluth Complex, Crystal Lake Intrusion); 2) high-tenor, disseminated to massive sulphide occurrences hosted by small 'early-rift' ultramafic intrusions (e.g. Eagle and Eagle East, Tamarack); 3) low-sulphide, PGE-enriched reef-style mineralization within well differentiated layered intrusions (e.g. Sonju Lake, Echo Lake); and 4) disseminated, sulphide-poor, PGE-Cu-enriched mineralization associated with 'early-rift' conduit-type ultramafic and mafic intrusions (e.g. Marathon Deposit, Current Lake, Sunday Lake). The reader is referred to Bleeker et al. (2020) and references therein for more detailed summaries of the key features of the various styles of Ni-Cu-PGE mineralization developed within the MCR.

In addition to refining the geochronological framework of the MCR magmatism and thus providing insights into the spatial and temporal controls on the various styles of ore formation, this TGI activity also characterizes the nature and timing of Ni-Cu-PGE mineralization within the Crystal Lake Intrusion to gain further insight into key ore-forming processes. The Crystal Lake Intrusion is an interesting case study as, unlike many other MCR Ni-Cu-PGE deposits, the mineralization shows a close spatial association with contaminated 'taxitic' rocks, a feature common in many other Ni-Cu deposits around the world, including the ores of Norilsk and Voisey's Bay[1]. This study combines field, petrographic, and mineralogical observations of the Crystal Lake ores, with high-precision U-Pb geochronology on various phases of the intrusion to examine/review (1) the role of contamination in ore formation; (2) the source and timing of S saturation; (3) the controls on the distribution of metals; and (4) the timing of ore formation relative to other MCR intrusions. This paper presents new field observations, mineralogical/laser ablation-inductively coupled plasma-mass spectrometry (LA-ICP-MS) results, and preliminary zircon and baddeleyite U-Pb ID-TIMS results for the Crystal Lake Intrusion and Mount Mollie dyke. The new ages begin to answer some unresolved questions regarding the timing of emplacement of the Crystal Lake Intrusion and its relationship to other MCR magmatic events, such as the Mount Mollie dyke, the north-northeast-trending Pigeon River dykes, and the Cu-Ni-bearing Duluth Complex. With a growing database of ages of MCR intrusions and continued efforts being made to refine the overall temporal framework of the MCR, we can start to delineate how ore formation relates in time and space to the overall evolution of the rift system and whether particular styles of mineralization are restricted to discrete magmatic episodes.

To gain insights into the behaviour and mobility of chalcophile elements during syn- and post-magmatic processes, we detail the mineral and trace element characteristics of precious metal-bearing minerals (PMM) and base metal sulphides within the Crystal Lake Intrusion. This has been achieved through combining a mineralogical deportment study with LA-ICP-MS analysis and element mapping. Although in the past metal deportment studies were largely utilized for optimizing metallurgical processing, they have also shown potential for applications to mineral exploration (e.g. Marathon deposit: Good et al., 2017). In addition, deportments also provide insights into the geological processes responsible for the concentration of metals, and thus ore formation (e.g. Holwell et al., 2006; Yudovskaya et al., 2011; Smith et al., 2014; Ames et al., 2017; Good et al., 2017) and are particularly insightful when combined with novel techniques such as quantitative LA-ICP-MS element mapping, which provides unparalleled spatial information at the microscopic scale.

GEOLOGICAL SETTING

The MCR represents a >2500 km arcuate tract of largely buried igneous and sedimentary rocks that extend from the Lake Superior region, where rift rocks are exposed, to the southwest and southeast (Van Schmus and Hinze, 1985; Stein et al., 2018). Geophysical anomalies, previously inferred as the Grenville Front, are now considered to represent the southward continuation of the MCR's eastern arm (Stein et al., 2018). Current U-Pb dates suggest that the extensive, plume-related, largely tholeiitic volcanism (~1.5 million km^3: Cannon, 1992) within the MCR was initiated at ca. 1109 Ma and continued intermittently to ca. 1083 Ma (Swanson-Hysell et al., 2019 and references therein). Geochronology of some of the intrusions (Heaman et al., 2007) may extend the onset of the main rift magmatism to ca. 1117 Ma (*see* Bleeker et al., 2018, 2020 for a detailed discussion). On the basis of existing geochronology and geochemical data, the MCR is conventionally divided into five stages: an initiation stage (ca. 1115–1109 Ma), an early stage (ca. 1109–1104), a latent stage (ca. 1104–1098 Ma), a main stage (ca. 1098–1090 Ma), and a late stage (ca. 1090–1083 Ma; Miller and Nicholson, 2013; Swanson-Hysell et al., 2019). The ca. 1144 Ma lamprophyre dykes and 1141 Ma Abitibi dyke swarm located to the northeast of Lake Superior are considered precursors to the main rifting event at ca. 1115 Ma (Krogh et al., 1987; Queen et al., 1996; Piispa et al., 2018). Although

[1] The close spatial association with taxitic-textured, hydrothermal mineral-rich marginal gabbro is also observed in basal mineralization of the Duluth Complex intrusions (J. Miller, pers. comm., 2019).

a number of dating studies have been undertaken on the MCR, there are continued efforts to improve and refine the temporal framework of the MCR magmatism. Recent studies include those by Bleeker et al. (2020), Swanson-Hysell et al. (2014, 2019), and Fairchild et al. (2017), which provide new high-precision chemical abrasion-ID-TIMS (CA-ID-TIMS) ages for both the MCR volcanic and intrusive rocks. The ongoing research by Bleeker et al. (2018, 2020) is continuing to refine the overall age distribution of the MCR magmatism, and as a result, previously anomalous ages (e.g. Inspiration sill, Pigeon River dykes, Current Lake Intrusion; Heaman et al., 2007; Smyk and Hollings, 2009) have now been constrained to within the ca. 1115–1084 Ma main rifting event. Furthermore, the new and refined ages of mineralized intrusions suggest that ore formation within the rift system was constrained to multiple episodes.

THE CRYSTAL LAKE INTRUSION

Geological Setting and Timing of Emplacement

The Crystal Lake Intrusion, located 47 km southwest of Thunder Bay, outcrops as a prominent Y-shaped body (Fig. 1) within the Animikie basin, intruding sulphur-bearing greywacke and mudstone of the Paleoproterozoic Rove Formation (Geul, 1970, 1973). Cross-sections, provided in Figure 2, illustrate the interpreted morphology of the intrusion, which is generally eastward plunging and thought to be lopolithic to dyke-like in shape. Whereas the northern limb has no strong magnetic expression, the southern limb is characterized by a magnetic anomaly. This could indicate that the intrusion extends deeper, potentially into a feeder dyke in the south (Fig. 2). Representative sections of the igneous stratigraphy of the northern and southern limbs are provided in Figure 3. Although the composition of the upper portion of the 'limbs' differs, both limbs are broadly comparable, characterized by a basal, sulphide-bearing vari-textured gabbro unit, overlain by a thick succession of homogeneous, unmineralized troctolite or magnetite-bearing olivine gabbro in the northern and southern limbs, respectively. With no chilled margin recognized at the upper contact of the mineralized vari-textured gabbros with the overlying barren troctolite/gabbro, which is represented by a distinct geochemical break, it is difficult to resolve the relative timing of these units. Fine-grained porphyritic diabase to coarse-grained, plagioclase-rich megacrystic sheet-like bodies, (Fig. 2, 3) intersect the Crystal Lake stratigraphy at depth. With a potential chilled margin recognized at the basal contact of the megacrystic sill (borehole CL003; Fig. 2, 3), these are thought to postdate emplacement of the main phases of the Crystal Lake Intrusion (however, see the comment in the caption to Fig. 2). For detailed petrographic descriptions of the Crystal Lake Intrusion, the reader is referred to Geul (1970), Mainwaring and Watkinson (1981), Smith and Sutcliffe (1987), Cogulu (1993a,b), Thomas (2015), and O'Brien (2018). Note that the geology of the Crystal Lake Intrusion is no longer subdivided into a basal, lower, middle/layered, and upper zones as defined in the earlier literature (Smith and Sutcliffe, 1987).

Geochemically, the Crystal Lake Intrusion can be distinguished from the more primitive conduit-type bodies of the MCR (e.g. Tamarack, Eagle), by olivine composition (Fo_{51-79}; Thomas, 2015; O'Brien, 2018), lower Ni/Cu and Pt/Pd ratios (<1), higher rare earth element (REE) abundances, light REE enrichment, and minimal fractionation of heavy REEs (Gd/Yb <2). In contrast to the high-grade, massive sulphide ores of Eagle and Tamarack, the mineralization at Crystal Lake is more comparable to the low-grade but extensive, disseminated ores of the Duluth Complex (Ripley 2014, and references therein).

At present, the timing of emplacement of the Crystal Lake Intrusion, which was previously dated at 1099.1 ± 1.2 Ma (Heaman et al., 2007), and its relationship with the MCRs north-northeast-trending Pigeon River dykes, the northwest-trending Cloud River dykes, the east- to northeast-trending Mount Mollie dyke, as well as the Duluth Complex, is poorly constrained (Fig. 1). This is largely resultant from poor exposure, lack of observed crosscutting relationships, and imprecise U-Pb ages. Based on Geul's (1970) interpretation, the Crystal Lake Intrusion crosscuts the Pigeon River dykes, which have been re-dated at ca. 1096.6 ± 2.2 Ma (Bleeker et al., 2020). With this notion supported by our own field observations and the apparent abrupt termination of Pigeon River dykes at the edge of the Crystal Lake Intrusion, the Heaman et al. (2007) age of 1099.1 ± 1.2 Ma may not reflect the true crystallization age of the Crystal Lake Intrusion. Newly recognized crosscutting relationships (Fig. 1), in addition to new U-Pb ages, indicate that the ca. 1097 Ma Pigeon River dykes post-date emplacement of the northwest-trending Cloud River dykes (Smith et al., 2019; Bleeker et al., 2020), which at ca. 1109 Ma may be related to the emplacement of the Logan sill complex. The Mount Mollie dyke, which comprises olivine gabbro, pegmatitic gabbro, and a granophyre core, is located immediately to the east of the Crystal Lake Intrusion. The relationship between these two intrusions has long been debated and, due to unreliable age constraints, remains unresolved. Although they have been suggested to be coeval (Smith and Sutcliffe, 1987; O'Brien, 2018), with Mount Mollie potentially representing a feeder dyke, this is not consistent with Hollings et al.'s (2010) reported baddeleyite age of 1109.3 ± 6.3 Ma. However, this older age is in dis-

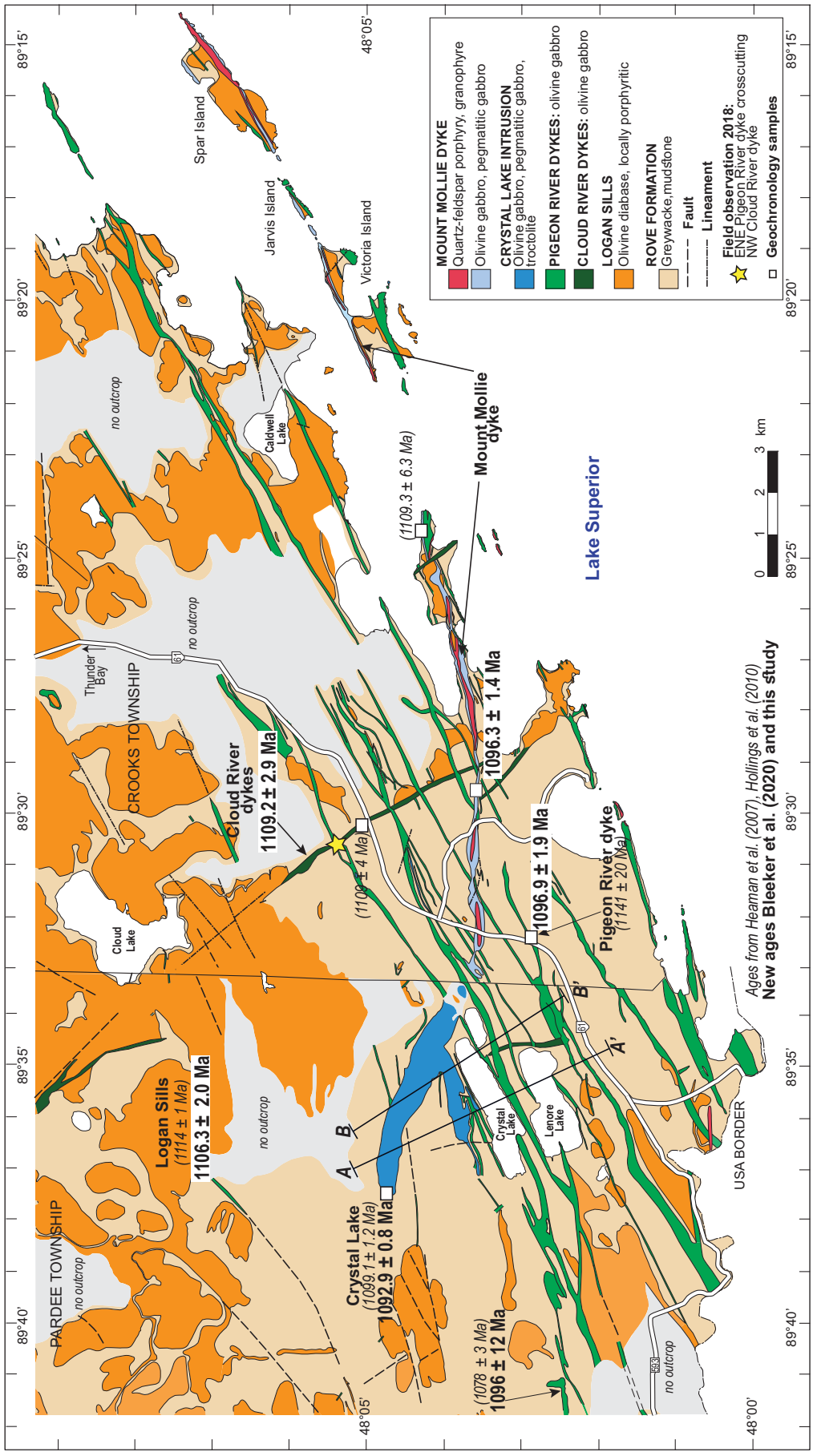

Figure 1. Geological map of Pardee and Crook townships showing the location and relationship of the Crystal Lake Intrusion with other Midcontinent rift intrusions. New U-Pb ages for the north-northeast-trending Pigeon River dykes, northwest-trending Cloud River dykes, and Logan sills (Bleeker et al., 2020) are shown, with previously determined ages by Heaman et al. (2007) and Hollings et al. (2010) in brackets. Map is *modified from* Geul (1970, 1973) on the basis of new field observations and age constraints.

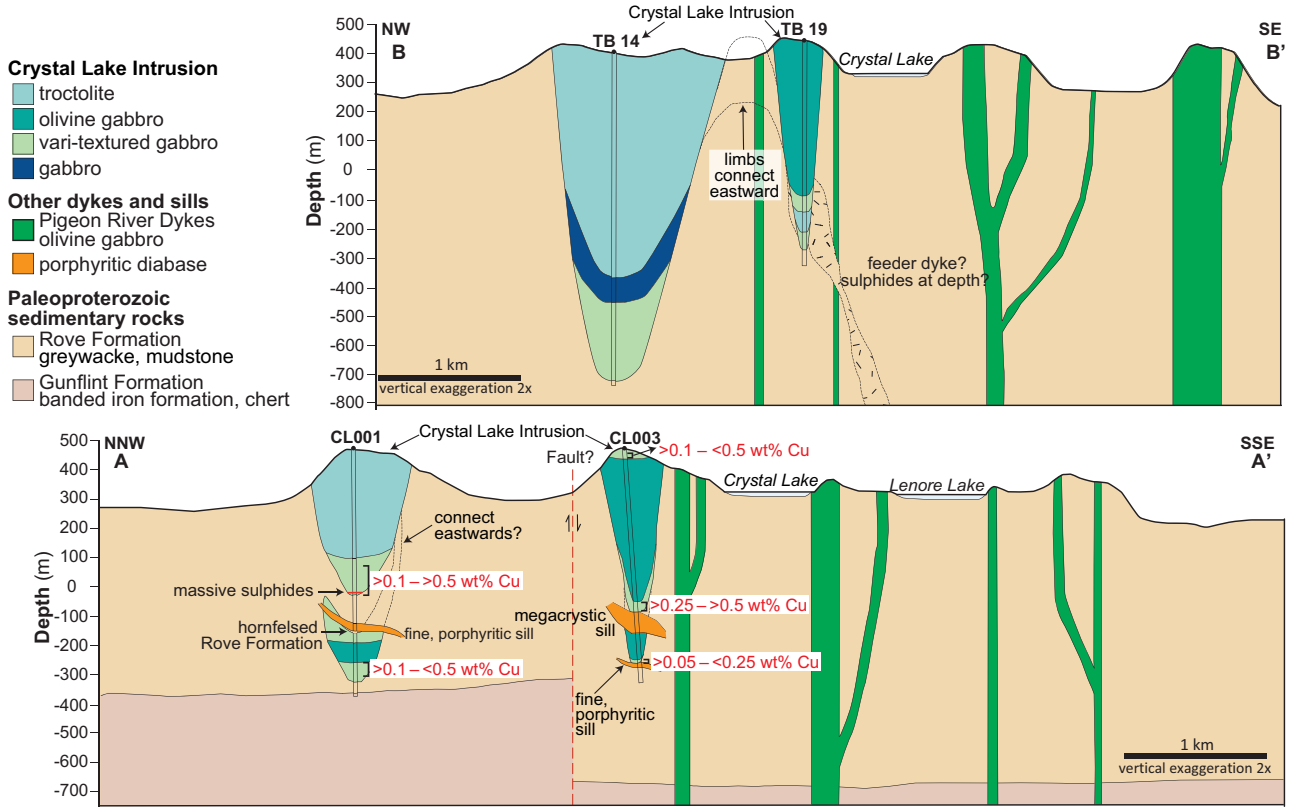

Figure 2. Cross-sections showing the interpreted morphology of the Crystal Lake Intrusion. Location of the sections are shown on Figure 1. Note that the "porphyritic diabase" units intersected at depth in section A-A' may be older Logan sills that predate the Crystal Lake Intrusion, rather than post-date the intrusion (J. Miller, pers. comm., 2019). No diabase sills in the area are known to be younger than the Crystal Lake Intrusion, whereas Logan Sills are abundant in the area.

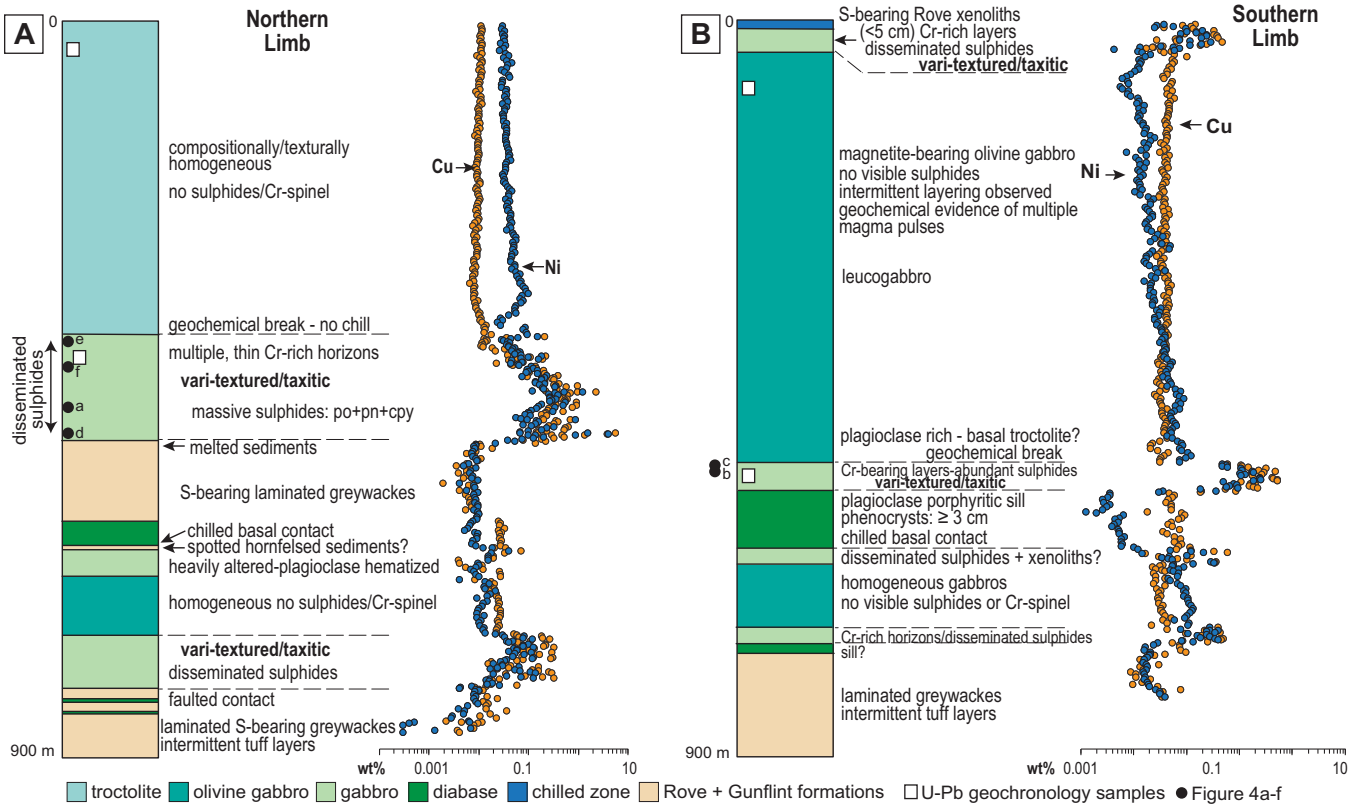

Figure 3. Representative stratigraphic columns of the **(a)** northern and **(b)** southern limbs of the Crystal Lake Intrusion. Metal concentrations from Goldner (2015, 2016). Location of geochronology samples and photographs provided in Figure 4 are also shown.

agreement with the normal polarity of the Mount Mollie dyke, a feature characteristic of younger rift rocks (<1100 Ma).

Vari-textured Gabbros: Textural Features

Vari-textured gabbros of the Crystal Lake Intrusion, referred to as 'taxites' in Norilsk literature (e.g. Lightfoot, 2007), are heterogeneous in nature, characterized by irregular variations in texture (fine-grained to pegmatitic) and composition, in addition to the presence of sulphides, Cr-spinel, and sedimentary/gabbroic xenoliths (Fig. 4). In the northern limb, discrete and sulphide-free troctolite layers are recognized near the upper contact of the vari-textured gabbro unit (Fig. 4f). These layers, which are comparable to the overlying troctolite unit, are in sharp (but not chilled) contact with the pegmatitic/vari-textured gabbros. The vari-textured gabbros also contain rare, spherical segregation vesicles (Fig. 5d). These vesicles are infilled with prehnite, biotite, amphiboles, and rare calcite, and are typically <1.5 cm in diameter. Although many of the segregation vesicles occur in association with sulphide droplets (*see* Discussion *below*), some occur without any sulphide attachment (Fig. 5d). Many deposits exhibit an association of sulphides with taxitic rocks, with the latter often interpreted to have crystallized from a volatile-rich, highly contaminated magma indicating significant wall-rock interaction (e.g. Norilsk, Voisey's Bay, Merensky Reef; Barnes and Campbell, 1988; Lightfoot, 2007; Cawthorn, 2010; Barnes et al., 2016).

Within the Crystal Lake Intrusion, Cr-spinel is found in association with the vari-textured gabbros, occurring as discrete, massive layers and stringers (<1 to ~100 cm thick) with sharp and diffuse contacts, and as irregular patches and xenoliths with both sharp and angular contacts (Fig. 4c, 5b,c,g). Cr-spinel also occurs as fine disseminations within the gabbroic rocks. The Cr-spinel layers are often brecciated and heterogeneous in appearance (Fig. 4c), containing sulphide-bearing and sulphide-free gabbro xenoliths and lenses (often elongated) of anorthositic material. Disseminated interstitial, blebby and globular sulphides are identified within the Cr-rich rocks. From the boreholes studied, it appears that the distribution of Cr-spinel differs between the two limbs of the intrusion. Within the northern limb, Cr-spinel primarily occurs as fine disseminations and as thin (<10 cm thick), undisturbed layers/stringers that do not contain significant sulphide mineralization and are associated with the upper portion of the vari-textured gabbro unit. In contrast, the southern limb vari-textured gabbros are characterized by thicker (<1 m), denser, Cr-spinel layers that are massive in nature, brecciated, and contain abundant sulphides (e.g. Fig. 4c). Towards the upper contact of the taxitic gabbros in the southern limb, the Cr-spinel horizons decrease in thickness and irregular Cr-rich patches/xenoliths are recognized (Fig. 5b).

Sedimentary xenoliths, some of which contain disseminated sulphides, are common near the margins of the intrusion (Fig. 5a; Geul, 1970, Mainwaring and Watkinson, 1981). They are irregular in shape with rounded contacts and are often characterized by an altered and sulphide-bearing rim. Interaction of the Crystal Lake magma(s) with the Rove Formation is also indicated by the high $\delta^{34}S$ signature of the Crystal Lake sulphides ($\delta^{34}S$ +1.4 to +21‰; Thomas, 2015; O'Brien, 2018) and the higher than mantle S/Se ratios (2850–4350; Eckstrand and Hulbert, 1987), which suggests a significant crustal S component throughout the ores. Mafic fragments, which are rounded to angular, are commonly identified within the vari-textured gabbros and Cr-spinel bearing horizons (Fig. 4a,b, 5e–g). Within the northern limb, these fragments are sulphide-free; however, in the southern limb sulphide-bearing and sulphide-free fragments are observed.

Ni-Cu-PGE Mineralization: New Petrographic Observations

Within the Crystal Lake Intrusion, sulphide mineralization is largely disseminated, with massive sulphide intervals (<50 cm thick) intersected locally within the northern limb (Fig. 4b–d). The disseminated ores, which are hosted by the vari-textured gabbros and Cr-bearing horizons, are variable in texture (Fig. 4a–c) with globular (silicate capped and uncapped), blebby, and interstitial sulphides identified. Globular sulphides (represented by sulphide aggregates that are convex and subspherical; Barnes et al., 2017, 2019) are irregularly distributed throughout the mineralized horizons.

The sulphide ores are dominated by the magmatic assemblage pyrrhotite, chalcopyrite, pentlandite ±cubanite with minor primary magnetite (Fig. 6a,b) and accessory nickel arsenides (Fig. 6f). Within the disseminated ores, sulphide grains are composed primarily of pyrrhotite and/or chalcopyrite. Pentlandite occurs as granular grains within pyrrhotite, around the margins of the composite grains, or along the contact between pyrrhotite and chalcopyrite (Fig. 6a–d). Exsolution flames/fans of pentlandite within pyrrhotite are also observed and are preferentially concentrated along fractures (Fig. 6e,j). Within the blebby/globular ores, curved lamellar exsolutions of an iron sulphide phase are occasionally observed within pyrrhotite (e.g. Fig. 6d,j). In areas where chalcopyrite and cubanite occur adjacent to or around the margins of pyrrhotite, rounded relics of pyrrhotite are observed within the Cu-rich phases (Fig. 6c). Within pyrrhotite-dominated blebs, chalcopyrite is restricted to the margins of the grains. Chalcopyrite (with minor pyrrhotite) is also

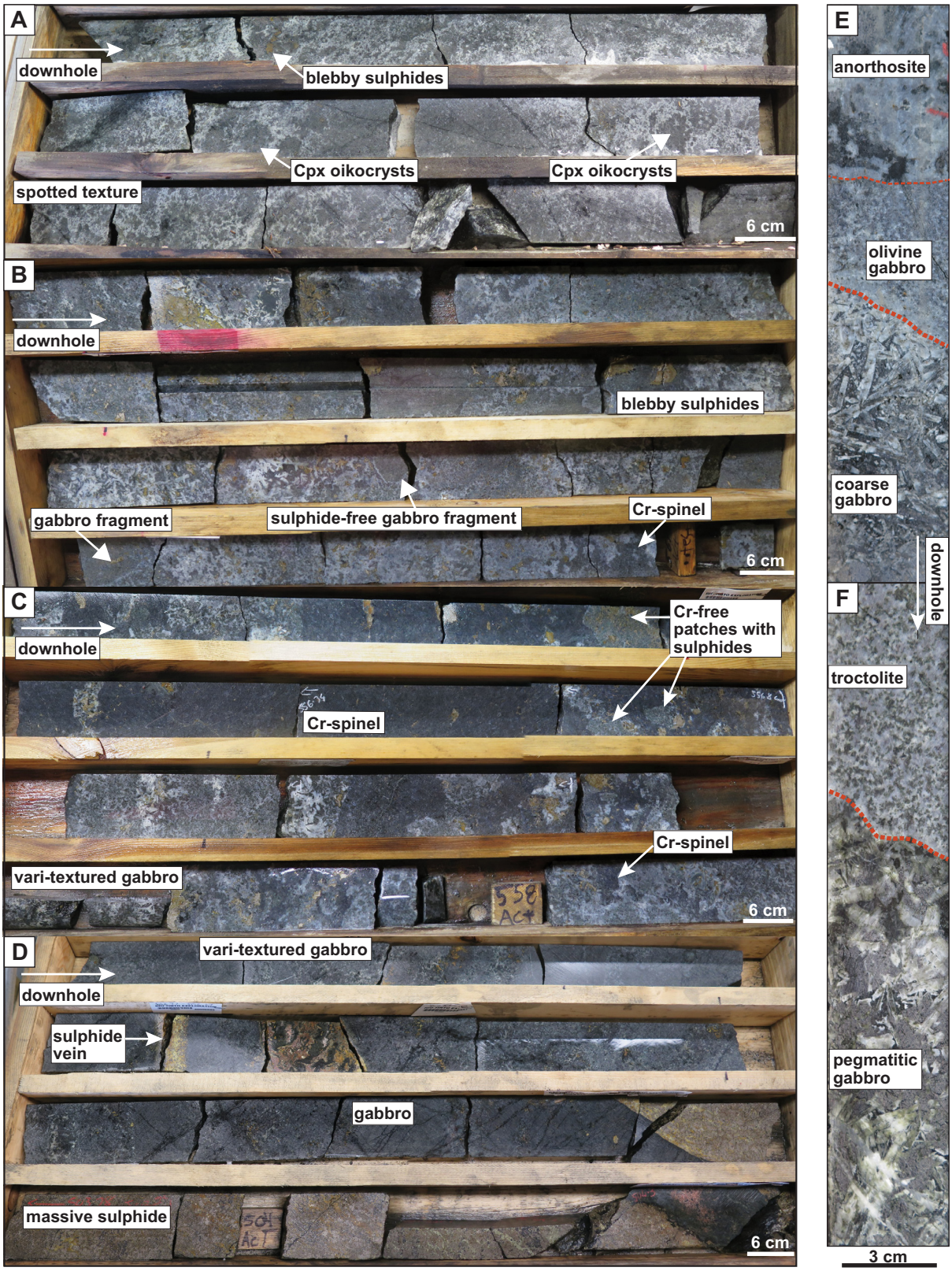

Figure 4. Representative photographs of Ni-Cu-PGE mineralization within the Crystal Lake Intrusion. **a, b)** Vari-textured gabbros from the northern limb, showing textural variations and associated interstitial/blebby sulphide mineralization. **c)** Chrome-spinel-rich horizon from the southern limb. Sulphide mineralization is disseminated and blebby in nature and is associated with the Cr-rich and Cr-free gabbro pockets. **d)** Massive sulphides developed within the northern limb. Note the sharp upper contact with gabbro and the presence of sulphide veins. **e)** Sharp layering observed near the upper contact of the vari-textured gabbro unit in the northern limb. **f)** Sharp contact observed between pegmatitic gabbro and troctolite near the upper contact of the vari-textured gabbro. Abbreviation: Cpx = clinopyroxene.

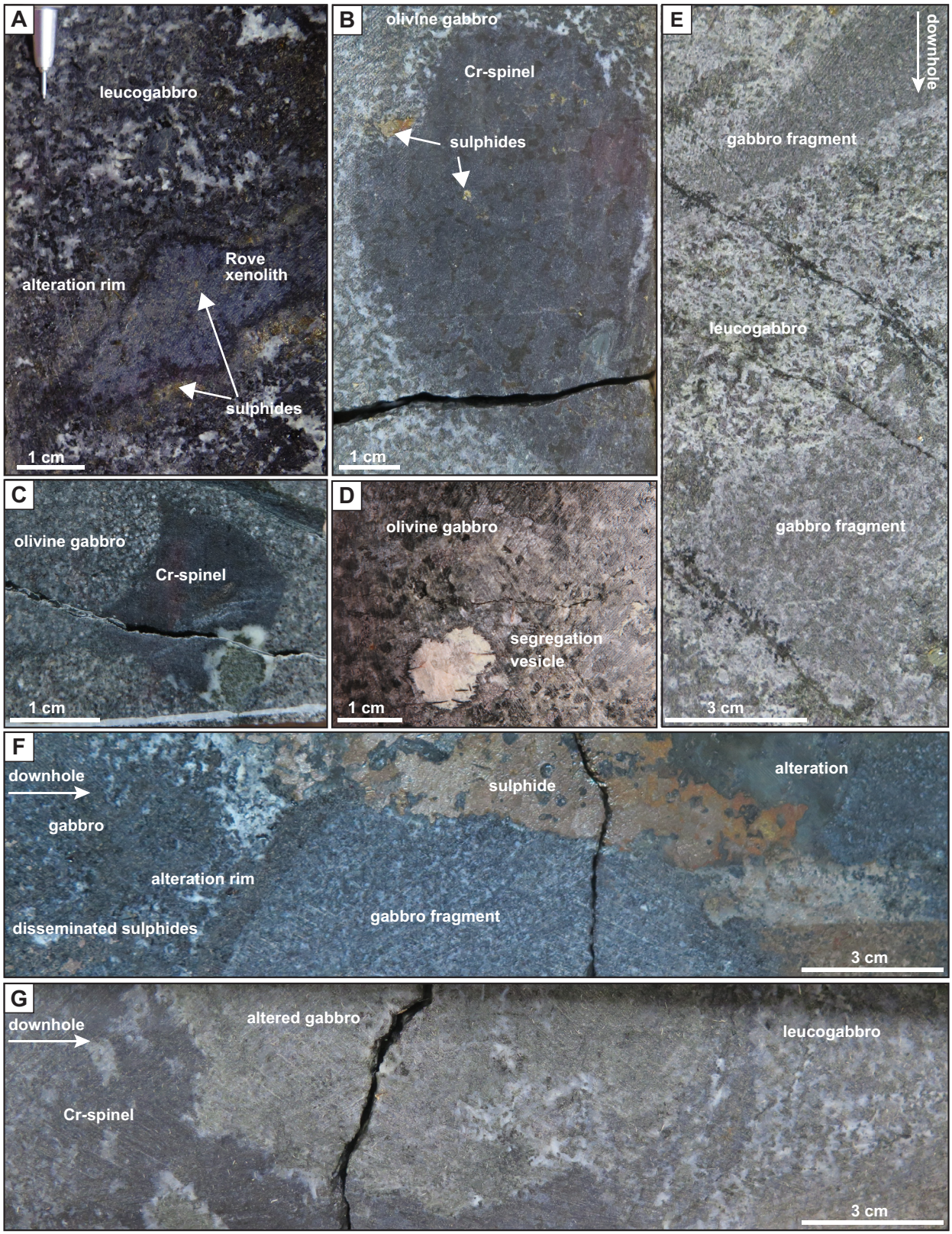

Figure 5. A representative selection of xenoliths/fragments observed within the Crystal Lake Intrusion. **a)** Irregular sedimentary xenolith within the Crystal Lake Intrusion; sulphides are abundant around the margin of the xenolith. **b)** Rounded chrome-spinel-rich xenolith with disseminated sulphides, within an olivine gabbro. **c)** Angular chrome-spinel clast within fine gabbro containing minor disseminated sulphides. **d)** Segregation vesicle composed of prehnite within an olivine gabbro from within the vari-textured gabbro unit. **e)** Textural variations commonly observation within the vari-textured gabbro units. **f)** A rounded gabbro fragment with massive sulphides and alteration around its margin. **g)** A rounded altered gabbro fragment, partially rimmed by chrome-spinel and hosted by leucogabbro.

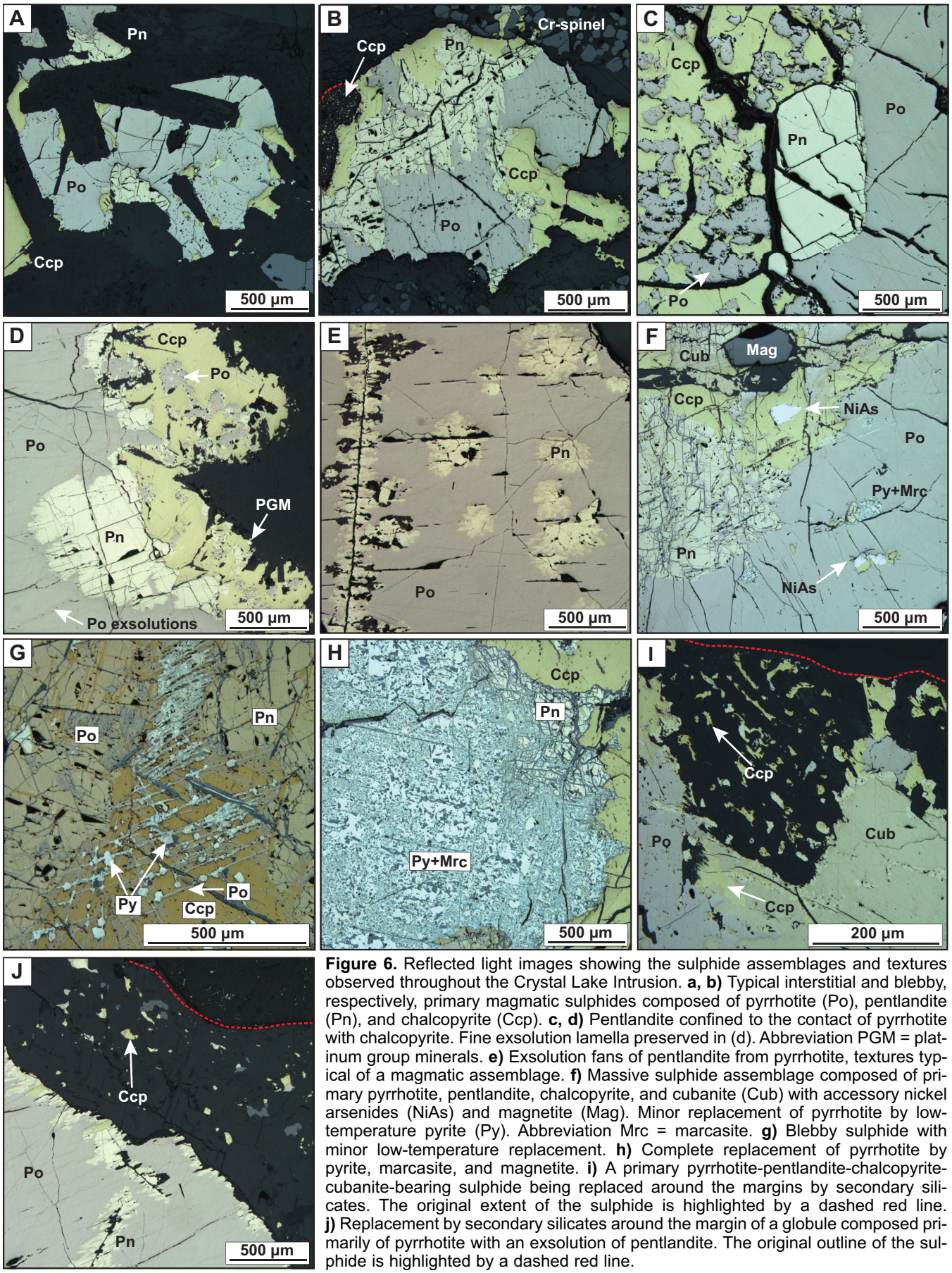

Figure 6. Reflected light images showing the sulphide assemblages and textures observed throughout the Crystal Lake Intrusion. **a, b)** Typical interstitial and blebby, respectively, primary magmatic sulphides composed of pyrrhotite (Po), pentlandite (Pn), and chalcopyrite (Ccp). **c, d)** Pentlandite confined to the contact of pyrrhotite with chalcopyrite. Fine exsolution lamella preserved in (d). Abbreviation PGM = platinum group minerals. **e)** Exsolution fans of pentlandite from pyrrhotite, textures typical of a magmatic assemblage. **f)** Massive sulphide assemblage composed of primary pyrrhotite, pentlandite, chalcopyrite, and cubanite (Cub) with accessory nickel arsenides (NiAs) and magnetite (Mag). Minor replacement of pyrrhotite by low-temperature pyrite (Py). Abbreviation Mrc = marcasite. **g)** Blebby sulphide with minor low-temperature replacement. **h)** Complete replacement of pyrrhotite by pyrite, marcasite, and magnetite. **i)** A primary pyrrhotite-pentlandite-chalcopyrite-cubanite-bearing sulphide being replaced around the margins by secondary silicates. The original extent of the sulphide is highlighted by a dashed red line. **j)** Replacement by secondary silicates around the margin of a globule composed primarily of pyrrhotite with an exsolution of pentlandite. The original outline of the sulphide is highlighted by a dashed red line.

present within thin veinlets, which are most commonly observed within the disseminated blebby/globular ores.

A low-temperature, alteration assemblage, characterized by pyrite, marcasite, chalcopyrite, and magnetite, is recognized in both the disseminated and massive sulphide ores. The degree of replacement of the primary assemblage is variable (e.g. Fig. 6f–h) with alteration more pervasive in the disseminated ores of the northern limb with increasing proximity to the basal footwall contact. The altered assemblages are texturally more complex and characterized by the partial to complete replacement of pyrrhotite and pentlandite by subhedral to euhedral pyrite, marcasite, and magnetite (Fig. 6f–h). In places, chalcopyrite contains crosscutting lamellae of pyrrhotite with which subhedral pyrite grains are associated with (Fig. 6g).

Alteration of sulphides by secondary silicates is largely confined to the margins of the grains and is a feature observed in both the primary and altered sulphide assemblages. The silicate alteration rim is variable in thickness and contains relics of pyrrhotite, pentlandite, chalcopyrite and magnetite (Fig. 6i,j). Platinum-group minerals also reside within these alteration halos.

Globular sulphides have been recognized in numerous intrusions, komatiites, and flood basalts including Sudbury, Norilsk, Black Swan, the Insizwa Complex, and dykes from East Greenland and Uruguay (Lightfoot et al., 1984; Dowling et al., 2004; Prichard et al., 2004; Holwell et al., 2012; Barnes et al., 2017, 2019; Le Vaillant et al., 2017). Within the Crystal Lake Intrusion, disseminated globular sulphides form only a minor component (Fig. 7). The lower contact of the globules is generally rounded with no evidence of the sulphide liquid infiltrating/penetrating downwards into the intercumulus framework. The globules are generally >1 cm in diameter and are composed of pyrrhotite and chalcopyrite with minor pentlandite. None of the globules investigated as part of the present study have experienced any low-temperature replacement by pyrite/marcasite. Internal differentiation of sulphide globules into a Cu-rich upper zone and Cu-poor, Ni-rich lower zone is commonly observed (e.g. Fig. 7a,d). Pentlandite is predominantly confined to the contact between chalcopyrite and pyrrhotite or the margins of the sulphide grains.

Silicate-capped globules have been documented in various intrusions and komatiitic bodies (e.g. Norilsk, Black Swan, macrodykes in East Greenland; Barnes et al., 2017 and references therein), and have been interpreted as remnants of a former magmatic vapour phase (Barnes et al., 2017). Silicate caps are also recognized in association with globular sulphides in the Crystal Lake Intrusion (Fig. 7c–f). The polymineralic caps are

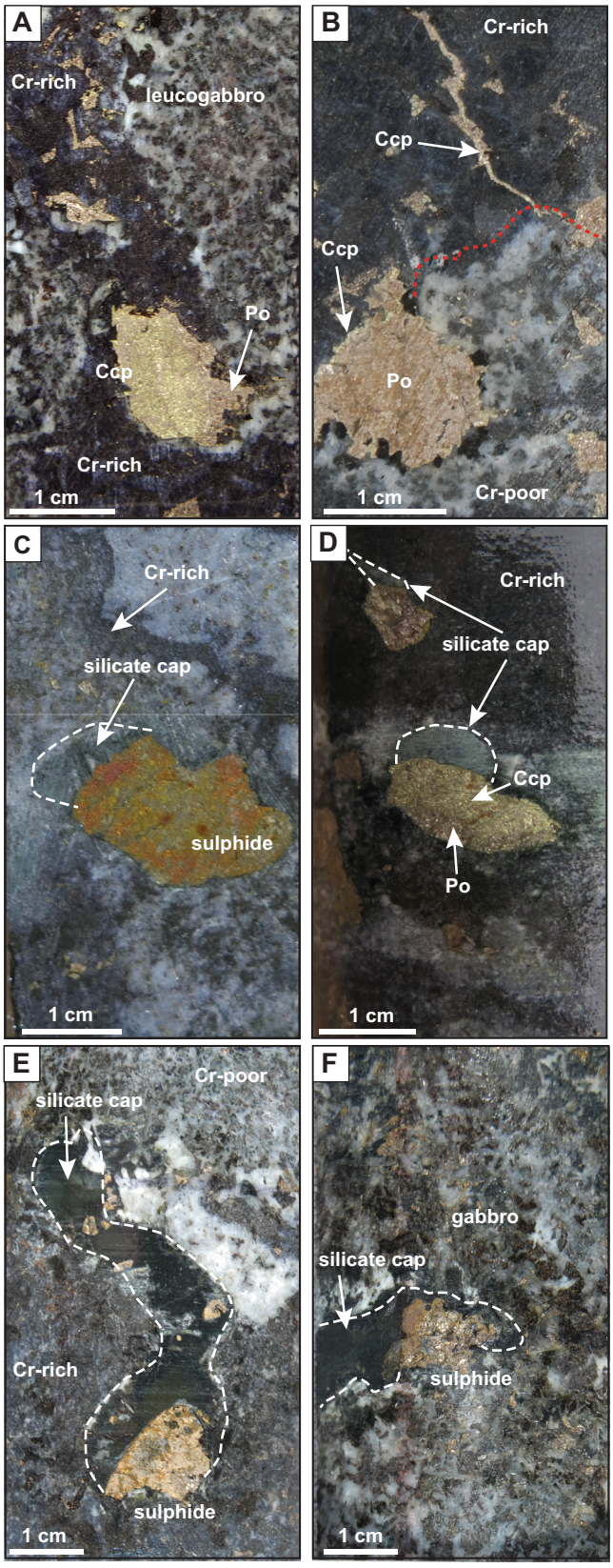

Figure 7. Examples of globular sulphides observed within the Crystal Lake Intrusion. **a, b)** Uncapped, sulphide globules within chrome-spinel-bearing horizons. **c, d)** Capped globules with regular silicate attachments. **e, f)** Capped sulphide globules with irregular-shaped attachments. Abbreviations: Ccp = chalcopyrite, Po = pyrrhotite.

Table 1. Preliminary U-Pb results for the Crystal Lake Intrusion and Mount Mollie dyke.

#	Description	Sample Number	Sample type/ Borehole/ Depth	Easting	Northing	Details	Age (Ma)
1	Northern limb Homogeneous, medium troctolite, unmineralized	18-SYB-001	drillcore CL0001 21–35 m	305453.19	5328330.35	Ab z, n=2, wm 7/6	1091.4 ± 1.4
2	Northern limb Vari-textured gabbro, minor sulphides, and Cr-spinel	18-SYB-002	drillcore CL0001 412–417 m	305453.19	5328330.35	Ab z, n=2, b, n=2, wm 7/6	1093.2 ± 1.2
3	Southern limb Coarse, vari-textured gabbro, minor sulphides, and Cr-spinel	18-SYB-111	drillcore CL0003 556–562 m	306239.91	5326523.72	Ab z, n=2, wm 7/6	1094.1 ± 1.4
4	Coarse, pink granophyre from centre of dyke	18-SYB-149	outcrop	313981.00	5325871.74	Ab z, n=2, bd=5, upper intercept	1096.3 ± 1.4

Abbreviations: Ab z = abraded zircon, bd = baddeleyite, n = number of fractions, wm 7/6 = weighted mean $^{207}Pb/^{206}Pb$ age.

completely filled with secondary amphibole, prehnite, and biotite, with accessory calcite and apatite. In comparison to the segregation vesicles described in the Norilsk ores, no primary magmatic phases have been recognized within the caps (Barnes et al., 2019). The silicate caps are typically attached to the upper margin of the sulphide bleb (Fig. 7c–e), although some droplets appear to be fully surrounded/encased by a secondary silicate halo. The morphology of the vapour phase is variable. Spherical, convex-up silicate caps, identical to those modelled by Mungall et al. (2015), are present (Fig. 7c,d) along with very irregular silicate attachments (Fig. 7e,f).

PRELIMINARY U-Pb RESULTS

New U-Pb results for the Crystal Lake Intrusion and Mount Mollie dyke are presented below. Note that many of these ages are preliminary, with additional analyses still in progress. The results of the four samples are summarized in Table 1. The reader is referred to Appendix 1 for details on U-Pb methods, and to Appendix 2 for a table of complete analytical data. Three samples from the Crystal Lake Intrusion were dated to determine (1) whether any age difference exists among the different phases and limbs; and (2) the relationship of the intrusion with the Pigeon River dykes and Mount Mollie dyke.

Crystal Lake Intrusion

The three samples from the Crystal Lake Intrusion yielded abundant, high-quality, fresh baddeleyite and magmatic zircon. For each sample, a population of the best quality, clear, and generally anhedral to subhedral zircon grains were selected for chemical abrasion pretreatment. Two single zircon grains of roughly prismatic form were analyzed for each sample and produced overlapping, concordant results, with good agreement among all three samples (Table 1, Fig. 8a–c). The mineralized vari-textured gabbro from the northern limb (sample 18-SYB-002; Fig. 8b) also includes the analyses of two multigrain baddeleyite fractions. Here, the baddeleyite data are concordant and show a high degree of overlap with the zircon data, producing a combined weighted average $^{207}Pb/^{206}Pb$ age of 1093.2 ± 1.2 Ma (Fig. 8b). Concordant zircons from the mineralized horizon of the southern limb yield a comparable weighted average $^{207}Pb/^{206}Pb$ age of 1094.1 ± 1.4 Ma (mean square weighted deviation (MSWD) = 2.6; Fig. 8c). The zircon data from the upper, unmineralized, homogenous troctolite unit is also concordant, producing a weighted average $^{207}Pb/^{206}Pb$ age of 1091.4 ± 1.4 Ma (MSWD = 1.3; Fig. 8a).

Combined U-Pb results for the best, concordant zircon and baddeleyite data from the three samples (including the following six fractions: 18-SYB-001 Z2; 18-SYB-002 Z1, Z2, B1, B2; and 18-SYB-111 Z2; Appendix 2) are presented in Figure 8d. They yield a weighted average $^{207}Pb/^{206}Pb$ age of crystallization of 1092.9 ± 0.8 Ma (MSWD = 0.55), and a concordia age (Ludwig, 2003) of 1092.3 ± 0.7 Ma. These new, preliminary ages are notably younger than the 1099.6 ± 1.2 Ma age reported by Heaman et al. (2007), which represents the weighted average $^{207}Pb/^{206}Pb$ age of the two more precise baddeleyite data points. Although less precise, Heaman's et al. (2007) upper intercept age of 1095.2 ± 3.7 Ma, overlaps within uncertainty with the new ages presented here.

Mount Mollie Dyke

A modest amount of zircon and baddeleyite crystals were recovered from sample 18-SYB-149, a coarse granophyre sampled from the centre of the Mount Mollie dyke on the mainland. Both the zircon and baddeleyite populations include altered grains of varying quality, with some of the zircon containing elevated

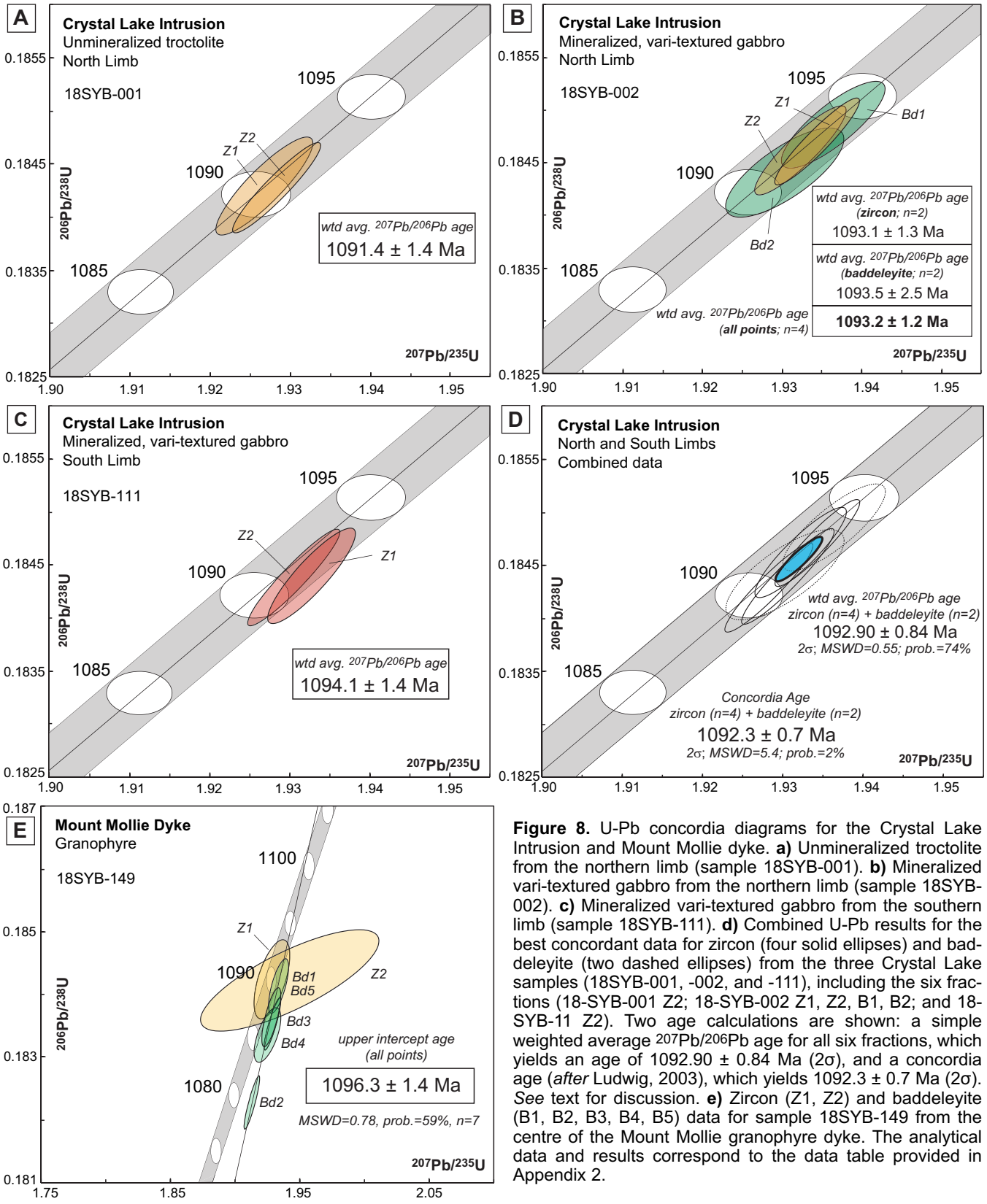

Figure 8. U-Pb concordia diagrams for the Crystal Lake Intrusion and Mount Mollie dyke. **a)** Unmineralized troctolite from the northern limb (sample 18SYB-001). **b)** Mineralized vari-textured gabbro from the northern limb (sample 18SYB-002). **c)** Mineralized vari-textured gabbro from the southern limb (sample 18SYB-111). **d)** Combined U-Pb results for the best concordant data for zircon (four solid ellipses) and baddeleyite (two dashed ellipses) from the three Crystal Lake samples (18SYB-001, -002, and -111), including the six fractions (18-SYB-001 Z2; 18-SYB-002 Z1, Z2, B1, B2; and 18-SYB-11 Z2). Two age calculations are shown: a simple weighted average $^{207}Pb/^{206}Pb$ age for all six fractions, which yields an age of 1092.90 ± 0.84 Ma (2σ), and a concordia age (*after* Ludwig, 2003), which yields 1092.3 ± 0.7 Ma (2σ). *See* text for discussion. **e)** Zircon (Z1, Z2) and baddeleyite (B1, B2, B3, B4, B5) data for sample 18SYB-149 from the centre of the Mount Mollie granophyre dyke. The analytical data and results correspond to the data table provided in Appendix 2.

common Pb. The two single zircon grains overlap in concordia space and straddle the concordia band (Fig. 8e). Fraction Z1 of sample 18SYB-149 is perfectly concordant with a $^{207}Pb/^{206}Pb$ age of 1089.6 Ma, whereas fraction Z2 is 1.5% discordant and yields a $^{207}Pb/^{206}Pb$ age of 1104.8 Ma, with the larger error associated with elevated common Pb. The five multi-grain, good quality, baddeleyite fractions are collinear

and, in this case, more precise than the zircon data. These fractions overlap concordia and yield an upper intercept age, anchored at 0 Ma, of 1096.4 ± 1.4 Ma (Fig. 8e). Together, the seven zircon and baddeleyite fractions (Z1, Z2, B1, B2, B3, B4, B5) have an upper intercept age of 1096.3 ± 1.4 Ma (MSWD = 0.78; Fig. 8e). This age is considerably younger than the previously reported age of 1109.3 ± 6.3 Ma (Hollings et al., 2010), which was a weighted average $^{207}Pb/^{206}Pb$ age from two less precise baddeleyite fractions.

PLATINUM GROUP MINERALOGY OF THE CRYSTAL LAKE INTRUSION

Over 8000 platinum group minerals (PGMs) and PMMs (total area of 1,625,255 μm^2) have been characterized. Results indicate that 91 to 99% of Pd is hosted by PMMs, with the rest residing in solid solution within sulphides. Platinum occurs almost exclusively (>99%) as discrete mineral phases. Precious metal-bearing minerals were successfully liberated when milled to P80 of 75 μm (80% material passing 75 μm), with the majority of grains occurring either completely free or attached to sulphides/silicates. Platinum-group minerals completely enclosed in sulphide or silicate phases were rare, although submicron PGM inclusions (too small to measure on the SEM) were commonly identified in nickel arsenide minerals.

The PMM assemblage of the Crystal Lake Intrusion is dominated by Pt-As (22%) and Pd-Pd±Sb±Te (41%)-bearing minerals. Of all PMMs classified, Pt- and Pd-bearing phases constitute 23% and 69% (by area), respectively. The PGMs and PMMs were grouped into seven types (in order of abundance by area): 1) Pd bismuthides (±Sb, ±Te); 2) Pt arsenides; 3) Pd/Pt-Sn±Sb minerals; 4) Pd antimonides; 5) composite grains; 6) Au-Ag minerals; and 7) Pd-nickel arsenides. Other minor mineral types identified (each constituting <1% of the assemblage) include Pd tellurides, Pd-Pt alloys (including rare Pt-Fe alloys), Pd bismuth-selenides, Pd/Pt bismuth-tellurides, and Rh/Ru sulphur-arsenides (Table 2). As recognized within many other Ni-Cu-PGE sulphide deposits, the PMMs reside in close proximity to sulphides (Fig. 9a–d). The PGMs typically occur (1) fully enclosed in sulphides, near the margins of the sulphide; (2) attached to sulphides; and (3) as satellite grains within secondary silicates surrounding sulphides (Fig. 9a–d).

The PMM assemblage of the Crystal Lake Intrusion is summarized in Table 2. By area, the most significant Pd-bearing minerals are unconstrained Pd-Bi-Sb±Te phases, froodite ($PdBi_2$), unconstrained Pd-Sn-Sb phases, stibiopalladinite (Pd_5+xSb_{2-x}), paolovite (Pd_2Sn), sobelevskite (PdBi), and electrum, all of which form >4% of the total PMM assemblage. Grains characterized by the exsolution of multiple minerals (Fig. 9e–h) were classified as composites and represent 5% (by area) of the total mineral assemblage. Composite grains, although variable in their mineralogy, are overwhelmingly dominated by the exsolution of froodite with unconstrained Pd-Bi±Sb±Te phases and Pd-Sb-Sn phases exsolved with electrum (Fig. 9f,h). Sperrylite ($PtAs_2$) represents the most important Pt-bearing phase. Platinum has also been identified as rare Pt-Fe alloys, rustenburgite ($(Pd,Pd)_3Sn$), and nigglite (PtSn).

The presence of abundant Cr-spinel does not appear to have any significant control over the mineralogy of PGMs, with the Cr-rich and Cr-poor samples characterized by near comparable PMM assemblages (Table 2, Fig. 10). A noticeable difference among the four samples studied is the greater abundance of PMMs identified in the Cr-bearing rocks of the northern limb, which have a total area of 659,555 μm^2, in comparison to <390,000 μm^2 in the other three samples. Furthermore this sample is also characterized by the abundance of Pd/Pt-Sn±Sb±As phases, which form 36% of the PMM assemblage. Elsewhere Sn-bearing phases represent only 0.6–3.2% of the overall mineral assemblage. Although the assemblages of the northern and southern limbs are broadly comparable, some subtle differences are recognized (Table 2, Fig. 10). Occurrences of Pd arsenides (e.g. palladoarsenide (Pd_2As) and unconstrained Pd-As phases), Pd tellurides, Pt-Pd alloys, and Pd bismuth-selenides (padmaite PdBiSe) are restricted to the northern limb assemblages (Table 2). The southern limb assemblages are characterized by Pd/Pt bismuth-tellurides (e.g. michenerite PdBiTe, maslovite PtBiTe), and Pd bismuth-arsenides and greater abundances of Pd-Ni arsenides (menshikovite $Pd_3Ni_2As_3$, majakite PdNiAs).

DISTRIBUTION OF ELEMENTS WITHIN SULPHIDES: LA-ICP-MS RESULTS

The precious metal and chalcophile element contents of sulphides from the Crystal Lake Intrusion, determined by LA-ICP-MS analyses, are summarized in Figure 11. The preliminary data show that the concentration of metals and trace elements is variable, not only between the primary sulphide phases but also among the different ore textures (i.e. contact, granular, and fan-textured pentlandite). Primary sulphide phases typically contain low concentrations of PGEs, with Os, Ir, and Pt, in addition to Au, measuring close to or below the limit of detection. Concentrations of Ru, Rh, and Pd are also low in pyrrhotite and chalcopyrite, but are elevated in pentlandite (>1–150 ppm Pd). The data suggests Mo, As, and Bi are preferentially concentrated in pyrrhotite and pentlandite (Fig. 11). Other elements, including Se, appear more comparable throughout the various sulphide phases.

Table 2. Summary of the platinum group minerals (PGMs) and precious metal-bearing mineral (PMM) assemblages (by area μm2) of the composite samples studied from the Crystal Lake Intrusion.

		Southern Limb		Northern Limb		Total Area
PMMs	Formula	Cr-rich	Cr-poor	Cr-rich	Cr-poor	
Pd bismuthides		***35,779***	***32,380***	***191,262***	***98,537***	**357,957**
Froodite	$PdBi_2$	35,087	28,384	128,545	96,771	
Sobelevskite	PdBi	692	3995	62,717	1765	
Pd-Bi-Sb±Te	unconstrained	***44,799***	***157,768***	***77,040***	***46,178***	***325,785***
Pt arsenide		***85,330***	***86,262***	***59,622***	***137,031***	***368,245***
Sperrlyite	$PtAs_2$	85,330	86,262	59,622	137,031	
Pd/Pt-Sn±Sb±As		***3320***	**2180**	***240,557***	***11,142***	***257,200***
Atokite	$(Pd,Pt)_3Sn$	25	765	474	158	
Palarstanide	$Pd5(Sn,As)_2$	1827	1324			
Paolovite	Pd_2Sn	516		102,629	1619	
Rustenburgite	$(Pt,Pd)_3Sn$		91			
Niggliite	PtSn				20	
Unconstrained	Pd-Sn-Sb	843		137,454	9345	
Unconstrained	Pd-Sn-As	109				
Pd antimonides±As		***37,295***	***76,049***	***26,026***	***4123***	**143,493**
Stibiopalladanite	$Pd_{5+x}Sb_{2-x}$	36,328	62,250	26,026	4123	
Sudburyite	$Pd_{0.75}Ni_{0.25}Sb$		13,528			
Isomertieite	$Pd_{11}Sb_2As_2$	232				
Mertieite	$Pd_{11}(Sb,As)_4$	225				
Unconstrained	Pd-Sb-As	510	271			
Composite		***10,740***	***2853***	***31,924***	***31,384***	**76,902**
Au-Ag minerals	Au(Ag)	***8507***	***15,453***	***28,563***	***15,527***	**68,050**
Pd nickel arsenides		***3581***	***6348***	***348***	***118***	**10,395**
Menshikovite	$Pd_3Ni_2As_3$	2433	2512	348		
Majakite	PdNiAs	1149	3836		118	
Pd bismuth-tellurides		***853***	***8234***			**9087**
Unconstrained	Pd-Bi-Te	507	617			
Michenerite	PdBiTe	346	7617			
Pd-Pt alloys				***3079***		**3079**
Zvyagintsevite	Pd_3Pb			2152		
Pt-Fe				928		
Pd-Bi-Se					***1641***	**1641**
Padmaite	PdBiSe				1641	
Rh/Ru sulphur-arsenides		***872***	***119***	***185***	***38***	**1214**
Hollingworthite	RhAsS	813	71	185	38	
Ruarsite	RuAsS	59	47			
Pd arsenides		***85***		***438***	***567***	**1090**
Stillwaterite	Pd_8As_3	85		119		
Palladoarsenide	Pd_2As			99	47	
Unconstrained Pd-As	Pd-As			220	520	
Sn oxide (Cassiterite)	SnO_2			***393***		**393**
Pt bismuth-telluride (Maslovite)	PtBiTe		***376***			**376**
Pd bismuth-arsenide	Pd-Bi-As	***39***	***114***			**153**
Unconstrained Pd-Bi-As						
Pd telluride (Keithconnite)	$Pd_{3-x}Te$ (x=0.14 to 0.43)			***118***		**118**
Bismuthide (Bismuthinite)	Bi_2S_3				***79***	**79**

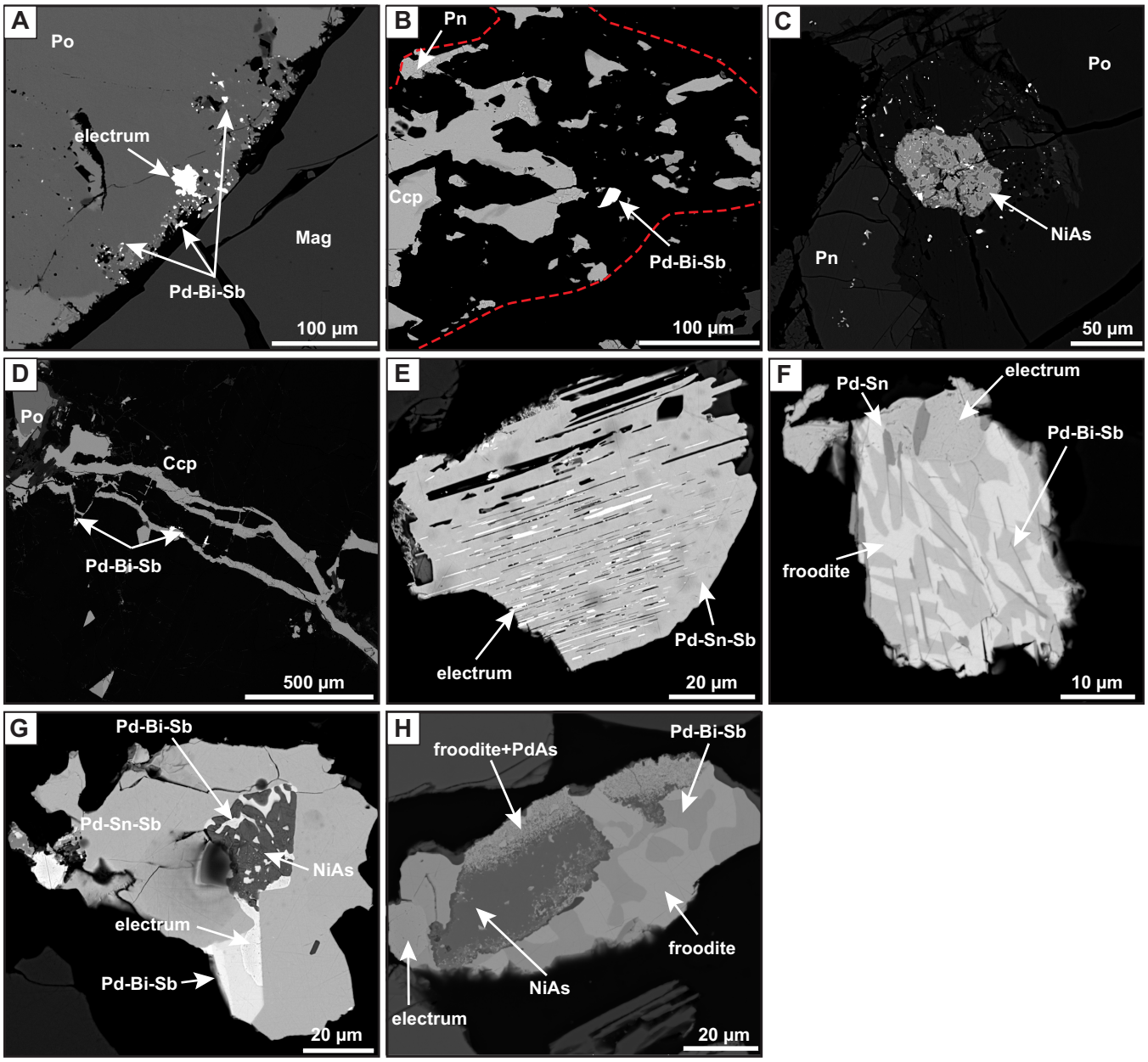

Figure 9. a–d) Back-scattered electron images showing the associations of precious metal-bearing minerals observed within the Crystal Lake Intrusion. **a)** A cluster of platinum group minerals (PGMs) and electrum enclosed within pyrrhotite, near the margin of a sulphide bleb. **b)** A PGM located within secondary silicates, in close proximity to a sulphide bleb. **c)** A cluster of PGMs occurring in close association with a nickel arsenide within the massive sulphide horizon. PGMs are also enclosed within pyrrhotite and pentlandite. **d)** PGMs associated with chalcopyrite veinlets. e–h) Back-scattered electron images of composite PGMs. **e)** Exsolution of electrum within a Pd-Sn-Sb-bearing mineral. **f)** Composite grain containing electrum (Au-Ag), froodite (PdBi2), Pd-Bi-Sb, and Pd-Sn phases. **g)** Pd-Sn-Sb-bearing mineral with electrum, Pd-Bi-Sb, and nickel arsenide. Note the inclusions of PGMs within nickel arsenide. **h)** A composite PGM grain associated with nickel arsenide. Note the fine-grained nature of the froodite and Pd-As-bearing phase occurring in association with the nickel arsenide. Abbreviations: Ccp = chalcopyrite, Mag = magnetite, Pn = pentlandite, Po = pyrrhotite,

Within the Crystal Lake Intrusion, pentlandite represents the main carrier of Pd in solid solution (>1–150 ppm) and accounts for 1–9% of the total Pd contents, with the rest residing in discrete PGMs. The Pd and trace element contents of pentlandite are variable among the massive, globular, and blebby sulphide ores (Fig. 11). The globular ores, which contain the lowest Co concentrations, are characterized by significantly elevated Pd concentrations (up to 150 ppm, mean 79 ppm). The blebby and massive ores, which contain comparable Co concentrations, contain <38 ppm and <3 ppm Pd, respectively. Though the globular and blebby ores appear to have similar As, Te, Bi, and Se contents, the massive ores are characterized by elevated Bi and As contents. The Pd content of the three distinct pentlandite textures (contact, granular, and fan;

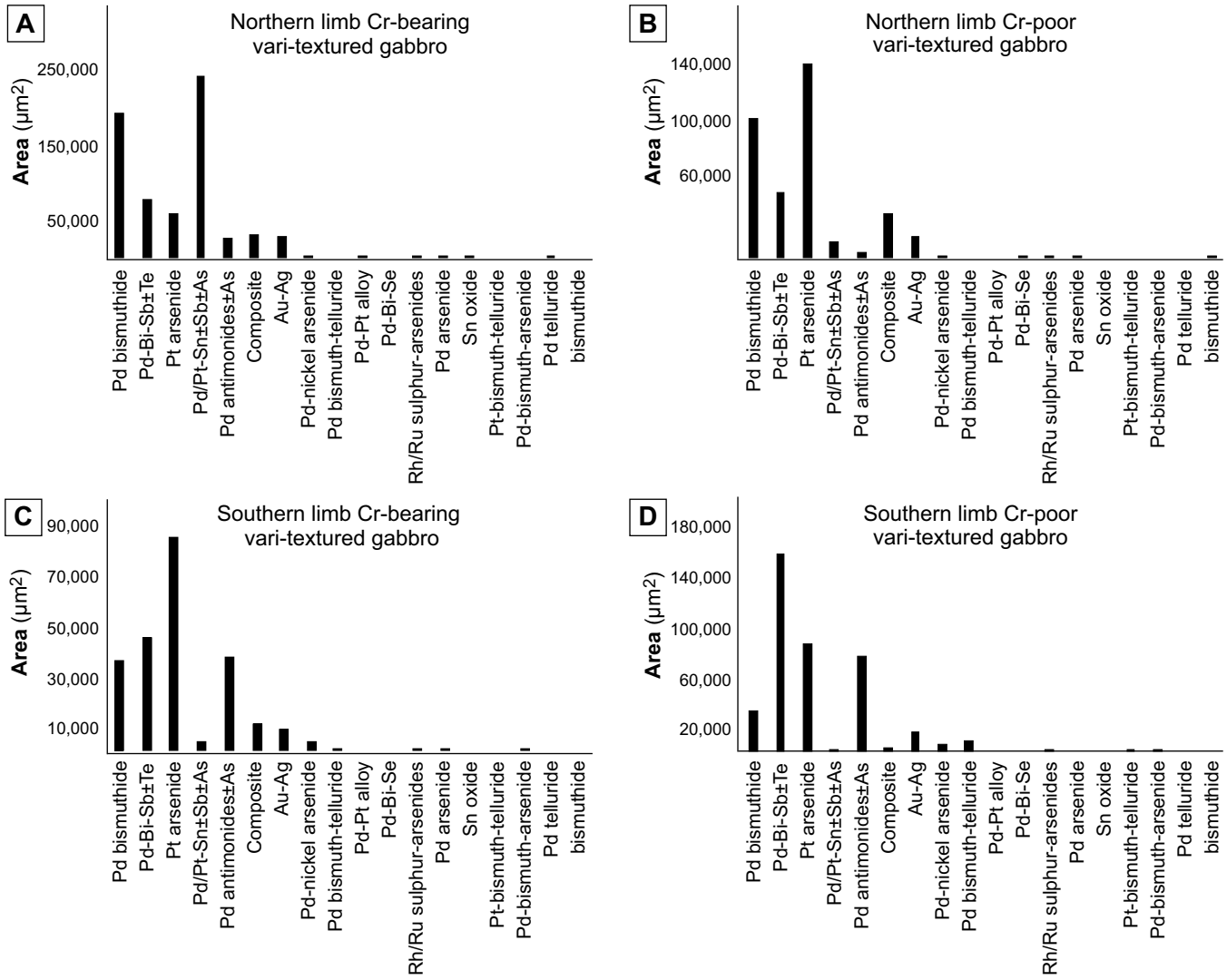

Figure 10. Histograms showing the platinum group mineral assemblage (by area): **a)** Cr-spinel-bearing rocks of the northern limb; **b)** vari-textured gabbros of the northern limb with no visible Cr-spinel; **c)** Cr-spinel bearing rocks of the southern limb; and **d)** vari-textured gabbros of the southern limb with no visible Cr-spinel.

Fig. 11) is variable. Palladium concentrations are noticeably elevated in the contact and granular pentlandite. Within a single sulphide droplet/bleb, the Pd contents of contact pentlandite are often elevated relative to granular or fan pentlandite.

Laser ablation ICP-MS imaging (Fig. 12) of the different sulphide ore textures, provides further insights into the spatial distribution of PGE and trace-elements at the microscopic scale. Within the unaltered primary magmatic assemblage, Pd is uniformly distributed within pentlandite regardless of its concentration (Fig. 12a,c,d). Pentlandite within the secondary sulphide assemblages is characterized by more heterogeneous element distributions (e.g. Pd, As, Bi; Fig. 12b) with evidence of remobilization of Pd and As, which appear to be broadly related. Complex zoning of several elements (e.g. As, Mo, Rh, Ru, Ir, and Re) is most commonly observed in pentlandite that is developed at the contact between pyrrhotite and chalcopyrite (Fig. 12a, c–d). These elements are depleted in pentlandite adjacent to the contact with chalcopyrite and enriched towards the pyrrhotite. Within some samples, the zonation is marked by a very distinctive, sharp boundary that clearly crosscuts the pentlandite grain (Mo in Fig. 12c). Although some zonation of Mo and Te are observed in chalcopyrite, elements are uniformly distributed throughout pyrrhotite, except where elements are preferentially concentrated into a microfabric.

A strong microfabric (Fig. 12d), which runs parallel to small micro-fractures, has been observed within some of the primary magmatic globular sulphides. The fabric is defined by several elements, including As, Mo, Pd, Re, Pb, Bi, V, and Cr, which appear to be preferentially concentrated along thin, parallel, linear features that are best developed within pyrrhotite and pentlandite (contact, granular, and fan), and occasionally extend into adjacent chalcopyrite. This fabric is not confined to a particular sulphide phase, with As, Mo,

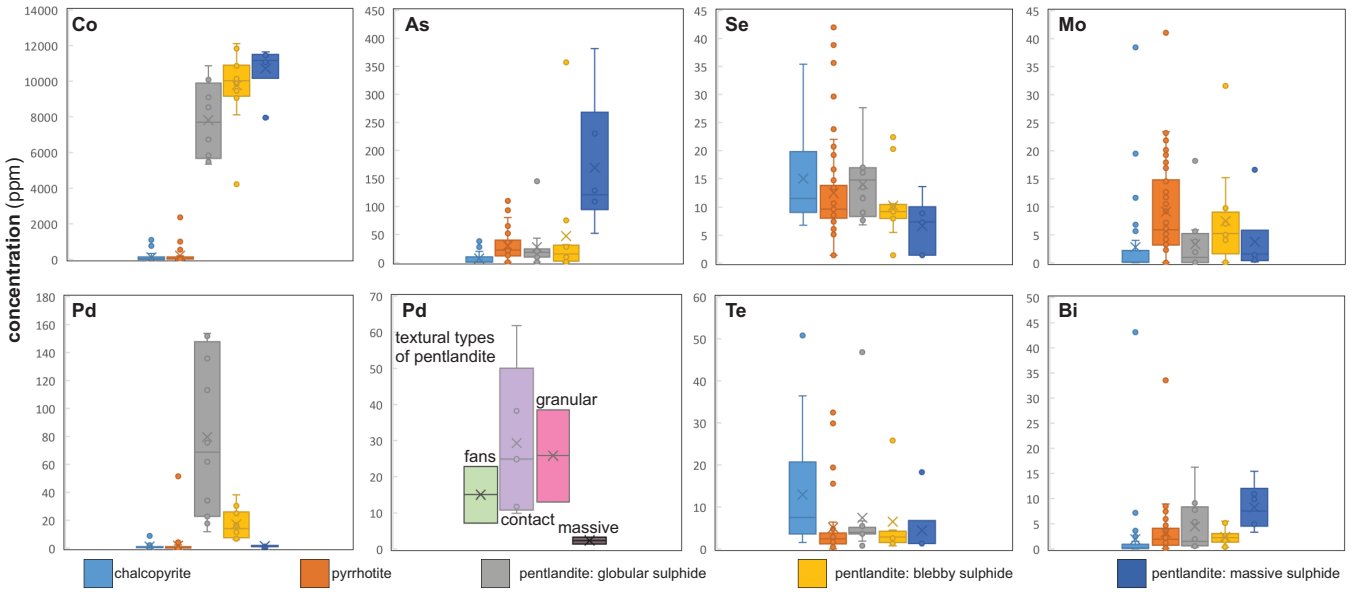

Figure 11. LA-ICP-MS results showing the compositional differences between the different sulphide phases. Palladium concentration for the various textures of pentlandite are also shown. The mean of the data set is represented by X.

and Re clearly crosscutting the primary sulphide contacts (Fig. 12d). This suggests preferential remobilization of these elements subsequent to fractionation of monosulphide solid solution (mss) and intermediate solid solution (iss). Late silicate-infilled fractures clearly cut the fabric as shown in the As map (Fig. 12d).

DISCUSSION

Emplacement of the Crystal Lake Intrusion and Mount Mollie Dyke

New ages for the Crystal Lake Intrusion and Mount Mollie dyke are not in agreement with those previously reported, therefore our data provide new temporal constraints for magmatism and ore formation within the MCR. The newly refined 1092.9 ± 0.8 Ma age for the Crystal Lake Intrusion is significantly younger than the previously reported age of 1099.6 ± 1.2 Ma (Heaman et al., 2007), and places it towards the end of the 'mainstage' of the rift's development. The Crystal Lake Intrusion thus appears to be the final intrusive pulse of a ca. 1097–1092 Ma magmatic episode that is represented by the dense Pigeon River swarm, the Mount Mollie dyke (*see below*), and the Beaver Bay Complex (*see* Bleeker et al., 2020). This magmatic episode is also well represented within the volcanic sequences of the North Shore and Portage Lake volcanic groups. The new ages confirm that the Crystal Lake Intrusion is not related to the ca. 1099 Ma Duluth Complex and northwest-trending Cloud River dykes (Bleeker et al., 2020). Furthermore, the age reported here is in better agreement with field observations, suggesting emplacement post-dates the ca. 1096 Ma north-northeast-trending Pigeon River dykes (Bleeker et al., 2020).

Our data also indicates that the Mount Mollie dyke is considerably younger than previously estimated (1109.3 ± 6.3 Ma; Hollings et al., 2010). Our new preliminary age of 1096.3 ± 1.4 Ma is now consistent with its normal polarity and suggests that it is coeval with the Pigeon River dyke swarm (Bleeker et al., 2020). Although the southern limb of the Crystal Lake Intrusion (sample 18-SYB-111) is just within error of the preliminary Mount Mollie age, our overall data suggests that these two intrusions are not directly related. Thus from the data currently available, Mount Mollie is thought to not be a feeder dyke to the Crystal Lake Intrusion. With additional zircon and baddeleyite analyses still in progress for both the Crystal Lake Intrusion and the Mount Mollie dyke, we hope to better resolve this relationship and provide a more refined (i.e. concordant) age for the latter.

From the newly refined ages presented here and in Bleeker et al. (2020), it is becoming increasingly apparent that the Ni-Cu-PGE mineralization is associated with multiple magmatic episodes throughout the evolution of the rift. Furthermore, ore formation appears to show a close temporal relationship with the various volcanic packages. From the current data, we are unable to conclude whether there is any evident age difference between the northern and southern limbs, or the unmineralized and mineralized phases of the Crystal Lake Intrusion, although there is a hint in the data that the unmineralized troctolite of the northern limb may be the youngest phase (compare Fig. 8a,b). Only additional high-precision analyses of well behaved zircons can settle this issue by reducing the errors on the weighted means to well below 1 Myr.

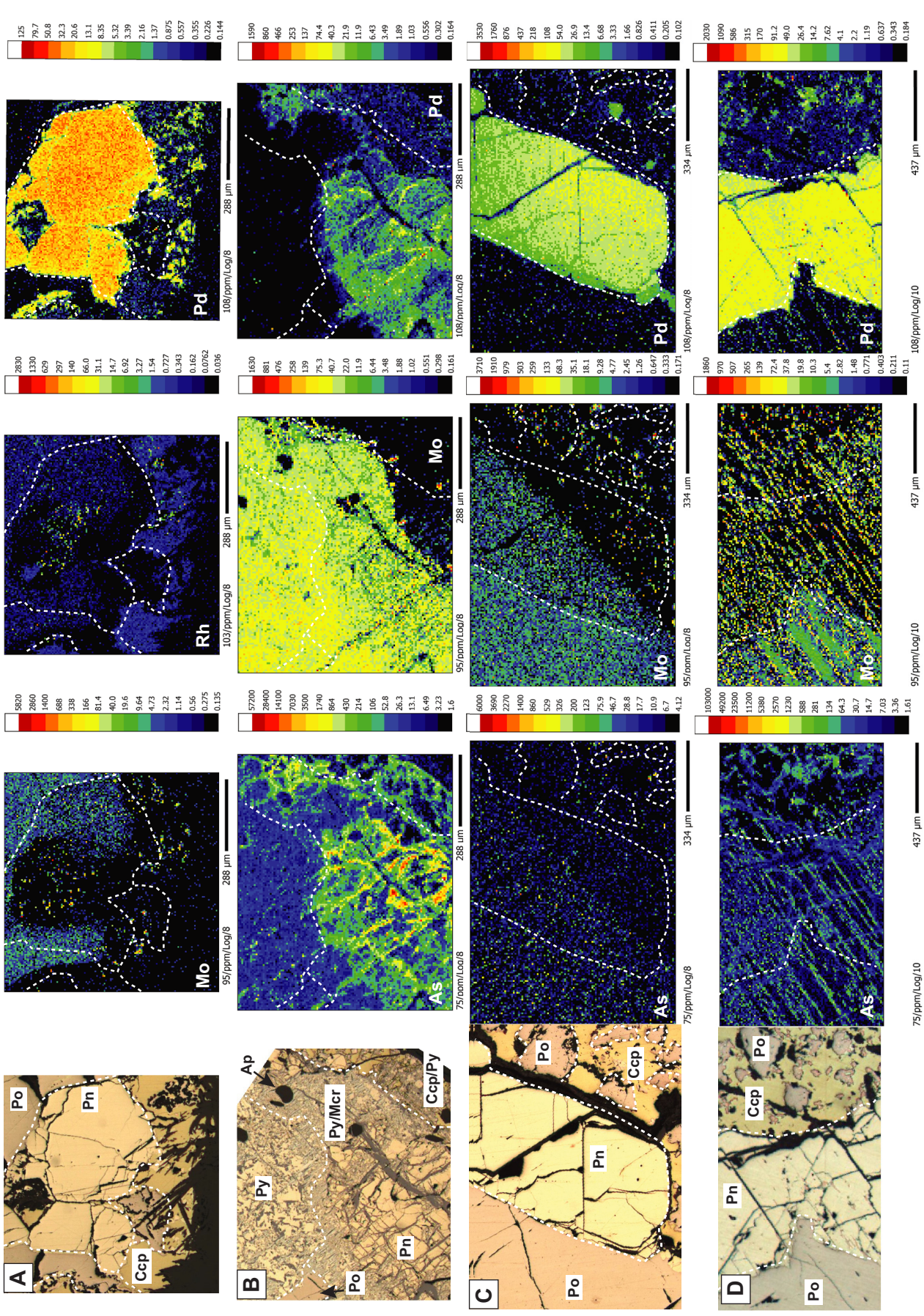

Figure 12. LA-ICP-MS element maps of primary magmatic **(a–c)** and **(d)** secondary sulphide assemblages. Abbreviations: Ap = apatite, Ccp = chalcopyrite, Mcr = marcacite, Pn = pentlandite, Po = pyrrhotite, Py = pyrite.

Conditions During Ore Formation: Sulphur Saturation, Contamination, and Volatiles

Within magmatic Ni-Cu-PGE sulphide systems, the addition of crustal S is considered critical for ore genesis. Although limited, S isotope data for the Crystal Lake Intrusion is consistent with the incorporation of significant sedimentary-derived S, with $\delta^{34}S$ values ranging from +1.4 to +21‰ (Thomas, 2015; O'Brien, 2018). The addition of crustal S has in the past been attributed to two key processes: 1) devolatilization and release of S from a thermal aureole; and 2) by direct melting and assimilation of wall rocks and sulphide-bearing xenoliths. After consideration of mass balance constraints and the time-scale of these processes, Robertson et al. (2015) concluded that S liberated from thermal aureoles is negligible in terms of ore formation, with dynamic wall-rock and xenolith melting being the most efficient and dominant mechanism for S transfer into the magma. With partially digested S-bearing xenoliths associated with the S-bearing taxitic rocks of the Crystal Lake Intrusion, in addition to a lack of any footwall control on the S isotopic data, we propose that crustal S was largely incorporated into the Crystal Lake magma through the melting of S-bearing xenoliths and wall rock, likely occurring both within the feeder dyke and during emplacement. Although S is available in the immediate footwall rocks, the heterogeneous nature of the S isotopic data set is more consistent with crustal S being derived distally relative to the final magma emplacement site. Therefore, like the Duluth Complex, the Crystal Lake Intrusion is interpreted to have been emplaced in S-saturated host rocks. Consequently, we therefore interpret the observed increase in S/Se ratios (Eckstrand and Cogulu, 1986) with proximity to the basal footwall contact as evidence of localized, in situ S contamination. This contamination event likely only contributed minor amounts of S into the system and is not considered critical for ore formation.

Within the Crystal Lake Intrusion, the contact of the mineralized taxitic rocks with the overlying unmineralized troctolite and olivine gabbro is marked by a distinct shift in the Cu/Pd ratio, from mantle-like signatures to greater than mantle or 'depleted' values (>10^4), respectively. The elevated Cu/Pd values within the upper, unmineralized units of both the northern and southern limbs, are consistent with PGE depletion of the magma through removal/segregation of sulphides. These ratios could indicate the early segregation of sulphides at depth, prior to final emplacement, as is also indicated by the preservation of large (>1 cm) globular sulphides (discussed below) and identification of 'ripped' sulphide clasts. Alternatively, the elevated Cu/Pd ratios could be indicative of in situ depletion of Pd through genesis of the underlying mineralization. This interpretation is only supported by several boreholes where a decrease in the Cu/Pd ratio towards the contact with the sulphide-bearing taxitic rocks is observed.

Constraining the initial source(s) of crustal S is extremely difficult within Ni-Cu-PGE systems as the transport and settling of xenoliths and the release of S is controlled by many factors (e.g. flow rate, temperature, density, size of xenoliths). Barnes and Robertson (2019), however, have recently shown that dissolution and melting rates of sulphide droplets and xenoliths, respectively, are slow relative to magma flow rates. The implications of this are that xenoliths, in addition to sulphide droplets, can be transported significant distances within a mafic system and that S can be released from the xenoliths both during transport and post-deposition. Considering the Crystal Lake Intrusion, it is feasible that the S-bearing sedimentary xenoliths (which were likely more buoyant than the carrier magma) were assimilated some distance (up to kilometres) from the final site of deposition. The observed association of mineralization, both with xenoliths and taxitic rocks, could suggest deposition of sulphide liquid together with the partially dissolved xenoliths, which continued to melt and release S (and volatiles) after deposition. As indicated by Barnes and Robertson (2019), this may provide some explanation for the close association of the ores, such as those at Crystal Lake, with contaminated/taxitic rocks.

Magmatic Ni-Cu-PGE sulphide deposits form in highly dynamic systems where there is prolonged magma flow (e.g. Lesher 1989; Bleeker, 1990a,b; Naldrett, 2004; Barnes et al., 2016). Continued recycling of the sulphide and thus multiple cycles of deposition, migration, re-entrainment, and re-deposition, are also thought to be critical in generating the high tenors of many deposits (e.g. Norilsk, Voisey's Bay). This notion is supported by computational fluid dynamic modelling, which shows that a segregated sulphide pool can be easily entrained back into the magma (Barnes and Robertson, 2019). At Crystal Lake, a degree of reworking is indicated by the presence of brecciated ores and fragments of Cr-spinel and gabbro within the taxitic units. Direct evidence of reworking of a deeper sulphide pool is potentially provided by the preservation of large sulphide droplets (>1 cm in size), which have been shown to be indicative of limited transport distance and thus proximity to a sulphide source or a reworked sulphide pool (Robertson et al., 2016). The internal differentiation (Cu-rich and Cu-poor) observed in many of these larger sulphide droplets (e.g. Fig. 7d) suggests that they were emplaced while molten, rather than being derived from a previously solidified sulphide liquid.

One of the more unique features of the ore-bearing taxites of the Crystal Lake Intrusion, is the presence of

segregation vesicles. Although vapour saturation and degassing are not common features of mafic Ni-Cu-PGE systems, segregation vesicles similar to those described here, have also been identified within the Norilsk ores, where they are interpreted to indicate shallow emplacement under low confining pressures (Barnes et al., 2019). The segregation vesicles within the Crystal Lake Intrusion could be interpreted to have formed under similar conditions. However, the lack of flattened bubble-droplet geometries, which Barnes et al. (2019) use as evidence for first boiling, in addition to the presence of irregular gas bubble attachments, and the identification of vesicles in the absence of sulphide could indicate that volatile saturation resulted from second boiling. Regardless of the timing of vapour saturation, it appears that within both the Norilsk and Crystal Lake Intrusions evidence of degassing is limited to the taxitic rocks, suggesting vapour saturation is favoured by the assimilation of volatile-rich sediments within these systems.

The role of volatiles within the Crystal Lake Intrusion and many other magmatic systems is indicated by the presence of distinctive pegmatitic-bearing units. Whereas the pegmatites of the Merensky Reef and other intrusions are interpreted to result from the crystallization of late-stage, ultra-fractionated volatile-rich material derived from trapped liquid in the cumulus pile (Barnes and Campbell, 1988), the marginal pegmatoidal units in the Norilsk intrusions, are thought to result from the local assimilation of volatiles during prolonged magma flow (Barnes et al., 2016). In the Crystal Lake Intrusion, taxitic rocks are widespread, occurring primarily at the margins of the intrusion and are thus also interpreted to be derived by local assimilation of volatile-rich sediments. Thermal modelling demonstrates that preheating of the basement facilitates partial melting and incorporation of volatiles into the magma (Karykowski et al., 2018), thus multiple magma influxes or prolonged flow are required to generate the significant volumes of pegmatitic material. The Crystal Lake Intrusion was therefore likely emplaced as a series of magmatic pulses, as suggested by Mainwaring and Watkinson (1981), Thomas (2015), and O'Brien (2018). Although the relationship of the taxitic rocks with the overlying unmineralized troctolites and olivine gabbros is not well constrained, preheating of the basement may have resulted from the earlier emplacement of these upper unmineralized units.

Controls on Metal and Trace Element Distributions

The distribution of PGEs within the Crystal Lake Intrusion, as revealed by detailed characterization of the PGM assemblages and LA-ICP-MS analyses, is consistent with the fractionation and crystallization of a magmatic sulphide liquid (Cabri and Laflamme, 1976; Fleet et al., 1993; Li et al., 1996; Ballhaus et al., 2001; Mungall et al., 2005; Holwell and McDonald, 2010). The abundance of Pd- and Pt-bearing PGMs, which account for >91% of these elements, in addition to the close association of PGMs with base metal sulphides, reflects the preferential partitioning of these elements from a fractionating sulphide liquid into a late-stage semi-metal-rich melt (Fleet et al., 1993; Helmy et al., 2007, 2010; Tomkins, 2010). The availability of Te, As, Bi, Sb, and Sn (referred to as TABS) within the magma and therefore the ability for a semi-metal-rich melt to fractionate from the sulphide liquid is thought to be primarily controlled by the assimilation of country rocks (Samalens et al., 2017). Although not significant to the overall metal budget at Crystal Lake, appreciable concentrations of Pd (<150 ppm) in pentlandite suggests that Pd was also concentrated within the fractionating sulphide liquid, which, upon cooling, was preferentially partitioned into exsolved pentlandite. For ore processing and extraction, the distribution of Pd and Pt primarily as PGMs in base metal sulphides is favourable for effective recovery as by-products of the Ni-Cu ores. Platinum group minerals hosted in sulphides rather than silicates are more easily liberated and are thus amenable for recovery by gravity concentration and flotation methods. For the Crystal Lake ores, we show that the majority of PGMs are liberated from their host when milled to P80 of 75 μm.

The PGM assemblage of the Crystal Lake Intrusion is dominated by varying proportions of Pd bismuthides, Pd-Bi-Sb-Te phases, Pt arsenides, and Pd antimonides (Table 2, Fig. 10). The observed similarity of the PGM assemblages of the northern and southern limbs suggests that the magma from which these ores crystallized was not distinct in its composition, and that the distribution and mineralogy of PGMs was controlled by the same processes throughout the intrusion. Furthermore, it is evident that the precipitation of Cr-spinel, which in some PGE-rich deposits (e.g. Merensky Reef) is known to effectively concentrate PGEs (Kinloch, 1982; von Gruenewaldt et al., 1989: Kinloch and Peyerl, 1990; Barnes and Maier, 2002; Godel et al., 2007), has no effect on the PGM assemblage in the Crystal Lake Intrusion. Whereas some variation in the proportion of the main PGM types is noted among the four samples studied: the Cr-rich ores of the northern limb are notably more abundant in Pd/Pd-Sn±Sb±As-bearing phases. This could potentially reflect a local footwall control. To understand whether the local footwall plays an important role in controlling the final PGM assemblage, a detailed comparison of MCR deposits hosted both within Paleoproterozoic sediments and Archean basement would be required.

The presence of significant concentrations of Pd in solid solution within pentlandite is a well documented feature of many Ni-Cu-PGE deposits (Norilsk, Voisey's Bay) and is considered a function of texture and therefore the temperature at which pentlandite exsolved (Piña et al., 2012; Mansur et al., 2019). Until recently, pentlandite was commonly interpreted to exsolve directly from mss, however, this model can not account for the preferential partitioning of Pd into pentlandite due to its incompatibility with mss (Liu and Brenan, 2015). Thus, a model that invokes some interaction/diffusion with the fractionating sulphide liquid is required (e.g. Piña et al., 2012; Mansur et al., 2019). Experimental studies have shown that a high-temperature Ni-rich phase can form via a peritectic reaction of mss with the fractionating sulphide liquid between 800 and 870°C (Waldner and Pelton, 2004; Kosyakov and Sinyakova, 2012; Kitakaze et al., 2016). This phase, which had previously not been documented in nature, is recognized in the Norilsk and Merensky ores by contact-style pentlandite that is characterized by zonation of Mo, Rh, Ru, Re, Os, and Ir along the pentlandite-chalcopyrite contact (Mansur et al., 2019). In the Crystal Lake Intrusion, three distinct textures of Pn are documented and referred to as contact, granular, and flame/fan. The homogeneous distributions of elements in granular and fan pentlandite, which contain comparable concentrations of Pd in a single sample, are interpreted to have exsolved from mss at <650°C and 200°C, respectively (Kelly and Vaughan, 1983). The depletion of Mo, Rh, Ru, and Re in the contact-style pentlandite along the contact with chalcopyrite (Fig. 12a,c,d) is consistent with Mansur's et al. (2019) observations and could be indicative of formation at ~870°C through peritectic reaction. Within a sulphide droplet, the elevated Pd concentrations in contact pentlandite relative to the lower temperature granular and fan textures support this interpretation and indicate partitioning of Pd, which is concentrated in the fractionated liquid into pentlandite during the peritectic reaction with mss.

The preferential concentration of various elements, including As, Mo, Pd, Re, and Bi into discrete linear features (Fig. 12d), is a rather interesting and unique feature of the Crystal Lake sulphide ores and is thought to be related to either sulphide fractionation, low-temperature alteration or deformation. Several observations indicate that the preferential remobilization of elements at the micro-scale occurred at low temperatures, post-sulphide fractionation: 1) the fabric is not confined to a single phase and crosscuts sulphide boundaries; 2) the fabric is preserved in high- and low-temperature pentlandite (contact, granular, and fans); 3) exsolutions within pyrrhotite do not correspond with the fabric; and 4) the linear features coincide with submicroscopic fractures. At this point, it is difficult to reconcile the exact process controlling the observed element distribution patterns. However, with the microfabric being restricted to globular droplets, and thus not being observed throughout the primary magmatic sulphide assemblage, this may indicate that it is a localized feature and not representative of a deposit-scale deformation event.

Like many other Ni-Cu-PGE deposits, the Crystal Lake ores have experienced some degree of low-temperature alteration, as indicated by the replacement of primary sulphides by low-temperature phases. The more heterogeneous distributions of Pd and As in the altered secondary sulphide assemblages (Fig. 12b) suggests these elements were locally remobilized during low-temperature alteration. The close association of PGMs with sulphides in addition to PGMs residing within silicate alteration halos around sulphides suggests remobilization was localized. This is further supported by whole-rock data, which shows strong positive correlations between Pd, Ni, Cu, and S (R = >0.7).

SUMMARY

The initial U-Pb results of this study indicate that the Crystal Lake Intrusion should now be considered as the youngest known mineralized intrusion within the MCR, representing the last intrusive phase of a major magmatic episode at ca. 1097 to 1092 Ma. This younger age suggests a correlation of the Crystal Lake Intrusion, not with the Duluth Complex, but rather with the younger intrusive phases of the Beaver Bay Complex.

The new field, petrographic, and mineralogical observations show that the Ni-Cu-PGE mineralization of the Crystal Lake Intrusion is broadly comparable to the ores of Norilsk, and are associated with reworked, volatile-rich, contaminated taxitic rocks that crystallized under low confining pressures. The similarity of the platinum group mineral assemblage, which is largely controlled by the availability of semi-metals through contamination, indicates crystallization from compositionally similar magmas. With evidence of reworking of the mineralized horizons and of a potentially deeper sulphide source/pool in the southern limb, the Crystal Lake ores appear to have formed in a more dynamic setting than previously thought and could possibly represent a conduit-type setting rather than a more stable intrusive environment. The addition of crustal S, through assimilation and melting of wall rocks and xenoliths prior to final emplacement, is considered critical for ore genesis. The local addition of S during emplacement is not considered critical for inducing S saturation. To gain a more comprehensive understanding of the timing of S saturation relative to emplacement, a more detailed S isotopic study of the intrusion is required.

With our new U-Pb results indicating that the Mount Mollie dyke is not a specific feeder to the Crystal Lake intrusion, we suggest that at least part of the feeder system may extend beneath the southern limb of the intrusion, which is characterized by a distinct magnetic anomaly.

ACKNOWLEDGMENTS

This report is a contribution to NRCan's Targeted Geoscience Initiative Program (TGI-5). Support for this study was provided through the Orthomagmatic Ni-Cu-PGE-Cr Ore Systems Project's 'Activity NC-1.3: Controls on the localization and timing of mineralized intrusions in intra-continental rift systems, with a specific focus on the ca. 1.1 Ga Midcontinent Rift system'.

The authors thank our partners at Rio Tinto (Dean Rossell, Brian Goldner) for providing access to drill core and constructive discussions. The Ontario Geological Survey, particularly Robert Cundari, Mike Easton, Mark Puumala, Mark Smyk, and Greg Paju, are also thanked for their logistical support throughout the 2018 and 2019 field seasons and for sharing their knowledge of the geology of the Thunder Bay area. We also thank Sarah Davey and Dustin Liikane for their assistance during fieldwork. Numerous discussions with Jim Miller, on the geology of the MCR, are acknowledged and have been beneficial. Similarly, his review of a draft of this report helped sharpen some points. Valérie Becu assisted with the technical editing and Elizabeth Ambrose took care of final editing and correction of minor imperfections. Both are thanked for their skillful assistance.

REFERENCES

Ames, D.E., Kjarsgaard, I.M., McDonald, A.M., and Good, D.J., 2017. Insights into the extreme PGE enrichment of the W Horizon, Marathon Cu-Pd deposit, Coldwell Alkaline Complex, Canada: platinum-group mineralogy, compositions and genetic implications; Ore Geology Reviews, v. 90, p. 723–747.

Ballhaus, C., Tredoux, M., and Spath, A., 2001. Phase relations in the Fe-Ni-Cu-PGE-S system at magmatic temperature and application to massive sulphide ores of the Sudbury Igneous Complex; Journal of Petrology, v. 42, p. 1911–1926.

Barnes, S.J. and Campbell, I.H., 1988. Role of late magmatic fluids in Merensky-type platinum deposits: A discussion; Geology, v. 6, p. 488–491.

Barnes, S.J. and Robertson, J.C., 2019. Time scales and length scales in magma flow pathways and the origin of magmatic Ni–Cu–PGE ore deposits; Geoscience Frontiers, v. 10, p. 77–87.

Barnes, S.J., Cruden, A.R., Arndt, N., and Saumur, B.M., 2016. The mineral system approach applied to magmatic Ni–Cu–PGE sulphide deposits; Ore Geology Reviews, v.76, p. 296–316.

Barnes, S.J., Mungall, J.E., Le Vaillant, M., Godel, B., Lesher, C.M., Holwell, D., Lightfoot, P.C., Krivolutskaya, N., and Wei, B., 2017. Sulfide-silicate textures in magmatic Ni-Cu-PGE sulfide ore deposits: Disseminated and net-textured ores; American Mineralogist, v. 102, p.473–506.

Barnes, S.J., Le Vaillant, M., Godel, B., and Lesher, C.M., 2019. Droplets and Bubbles: Solidification of Sulphide-rich Vapour-saturated Orthocumulates in the Norilsk-Talnakh Ni–Cu–PGE Ore-bearing Intrusions; Journal of Petrology, v. 60, p. 269–300.

Barnes, S.-J. and Maier. W.D., 2002. Platinum-group element distributions in the Rustenburg Layered Suite of the Bushveld Complex, South Africa; Canadian Institute of Mineralogy, Metallurgy and Petrology, v. 54, p. 553–580.

Begg, G.C., Hronsky, J.A., Arndt, N.T., Griffin, W.L., O'Reilly, S.Y., and Hayward, N., 2010. Lithospheric, cratonic, and geodynamic setting of Ni-Cu-PGE sulphide deposits; Economic Geology, v. 105, p. 1057–1070.

Bleeker, W., 1990a. Evolution of the Thompson Nickel Belt and its nickel deposits, Manitoba, Canada; Ph.D. thesis, University of New Brunswick, Fredericton, New Brunswick, 400 p.

Bleeker, W., 1990b. Thompson Area—General geology and ore deposits; *in* Geology and Mineral Deposits of the Flin Flon and Thompson Belts, Manitoba; *in* Field Trip no. 10 Guidebook, 8th IAGOD Symposium, p. 93–125.

Bleeker, W., Liikane, D.A., Smith, J., Hamilton, M., Kamo, S.L., Cundari, R., Easton, M., and Hollings, P., 2018. Activity NC-1.3: Controls on the localisation and timing of mineralized intrusions in intra-continental rift systems, with a specific focus on the ca. 1.1 Ga Mid-continent Rift (MCR) system; *in* Targeted Geoscience Initiative: 2017 Report of Activities, Volume 2, (ed.) N. Rogers; Geological Survey of Canada, Open File 8373, p. 15–27.

Bleeker, W., Smith, J., Hamilton, M., Kamo, S., Liikane, D., Hollings, P., Cundari, R., Easton, M., and Davis, D., 2020. The Midcontinent Rift and its mineral systems: Overview and temporal constraints of Ni-Cu-PGE mineralized intrusions; *in* Targeted Geoscience Initiative 5: Advances in the understanding of Canadian Ni-Cu-PGE and Cr ore systems – Examples from the Midcontinent Rift, the Circum-Superior Belt, the Archean Superior Province, and Cordilleran Alaskan-type intrusions, (ed.) W. Bleeker and M.G. Houlé; Geological Survey of Canada, Open File 8722, p. 7–35.

Cabri, L.J. and Laflamme, J.H.G., 1976. The mineralogy of the platinum-group elements from some copper–nickel deposits of the Sudbury area, Ontario; Economic Geology, v. 71, p. 1159–1195.

Cannon, W.F., 1992. The Midcontinent rift in the Lake Superior region with emphasis on its geodynamic evolution; Tectonophysics, v. 213, p. 41–48.

Cawthorn, R.G., 2010. The platinum group element deposits of the Bushveld Complex in South Africa; Platinum Metals Review, v. 54, p. 205–215.

Cogulu, E., 1993a. Factors controlling postcumulus compositional changes of chrome-spinels in the Crystal Lake intrusion, Thunder Bay, Ontario; Geological Survey of Canada, Open File 2748, 28 p.

Cogulu, E., 1993b. Mineralogy and chemical variations of sulphides from the Crystal Lake intrusion, Thunder Bay, Ontario; Geological Survey of Canada, Open File 2749, 21 p.

Dowling, S.E., Barnes, S.J., Hill, R.E.T., and Hicks, J., 2004. Komatiites and nickel sulfide ores of the Black Swan area, Yilgarn Craton, Western Australia. 2. Geology and Genesis of the Orebodies; Mineralium Deposita, v. 39, p. 707–728.

Eckstrand, O.R. and Cogolu, E., 1986. Se/S evidence relating to genesis of sulphides in the Crystal Lake gabbro, Thunder Bay, Ontario; Geological Association of Canada-Mineralogical Association of Canada, Abstracts, v. 11, p. 66.

Eckstrand, O.R. and Hulbert, L.J., 1987. Selenium and the source of sulfur in magmatic nickel and platinum deposits; Geological Association of Canada-Mineralogical Association of Canada, Abstracts,. v. 12, p. 40.

Fairchild, L.M., Swanson-Hysell, N.L., Ramezani, J., Sprain, C.J., and Bowring, S.A., 2017. The end of Midcontinent Rift magmatism and the paleogeography of Laurentia; Lithosphere, v. 9, p. 117–133.

Fleet, M.E., Chryssoulis, S.L., Stone, W.E., and Weisener, C.G., 1993. Partitioning of platinum-group elements and Au in the Fe–Ni–Cu–S system: experiments on the fractional crystallization of sulfide melt; Contributions to Mineralogy and Petrology, v. 115, p. 36–44.

Geul, J.J.C., 1970. Geology of Devon and Pardee Townships and the Stuart Location, District of Thunder Bay; Ontario Department of Mines, Geological Report 87, 58 p.

Geul, J.J.C., 1973. Geology of Crooks Township, Jarvis and Prince Locations, and Offshore Islands, District of Thunder Bay; Ontario Department of Mines, Geological Report 102, 46 p.

Godel. B., Barnes, S.-J., and Maier, W.M., 2007. Platinum-group elements in sulfide minerals, platinum-group minerals, and whole-rocks of the Merensky Reef (Bushveld Complex, South Africa) Implications for the formation of the reef; Journal of Petrology, v. 48, p, 1569–1604.

Goldner, B., 2015. Rio Tinto Exploration Canada Inc. Assessment Report on the Cu-Ni-PGE Crystal Lake Project. Pardee, Devon and Crooks Township, NTS 52A/04; Thunder Bay Mining Division, Ontario, 825 p.

Goldner, B., 2016. Rio Tinto Exploration Canada Inc. Assessment Report on the Cu-Ni-PGE Crystal Lake Project. Pardee, Devon and Crooks Township, NTS 52A/04; Thunder Bay Mining Division, Ontario, 219 p.

Good, D.J., Epstein, R., McLean, K., Linnen, R.L., and Samson, I.M., 2015. Evolution of the Main Zone at the Marathon Cu-PGE sulphide deposit, Midcontinent Rift, Canada: spatial relationships in a magma conduit setting; Economic Geology, v. 110, p. 983–1008.

Good, D.J., Cabri, L.J., and Ames, D.E., 2017. PGM facies variations for Cu-PGE deposits in the Coldwell Alkaline Complex, Ontario, Canada; Ore Geology Reviews, v. 90, p. 748–771.

Green, J.C., 1983. Geologic and geochemical evidence for the nature and development of the Middle Proterozoic (Keweenawan) Midcontinent Rift of North America; Tectonophysics, v. 94, p. 413–437.

Heaman, L.M., Easton, R.M., Hart, T.R., Hollings, P., MacDonald, C.A., and Smyk, M., 2007. Further refinement to the timing of Mesoproterozoic magmatism, Lake Nipigon region, Ontario; Canadian Journal of Earth Sciences, v. 44, p. 1055–1086

Helmy, H.M., Ballhaus, C., Berndt, J., Bockrath, C., and Wohlgemuth-Ueberwasser, C., 2007. Formation of Pt, Pd and Ni tellurides; experiments in sulfide-telluride systems; Contributions to Mineralogy and Petrology, v. 153, p. 577–591.

Helmy, H.M., Ballhaus, C., Wohlgemuth-Ueberwasser, C., Fonseca, R.O.C., and Laurenz, V., 2010. Partitioning of Se, As, Sb, Te and Bi between monosulfide solid solution and sulfide melt—application to magmatic sulfide deposits; Geochimica et Cosmochimica Acta v. 74, p. 6174–6179.

Hollings, P., Smyk, M., Heaman, L.M., and Halls, H., 2010. The geochemistry, geochronology, and paleomagnetism of dikes and sills associated with the Mesoproterozoic Mid-continent Rift near Thunder Bay, Ontario, Canada; Precambrian Research, v. 183, p. 553–571.

Holwell, D.A. and McDonald, I., 2010. A review of the behaviours of platinum group elements within natural magmatic sulfide ore systems; Platinum Metal Reviews, v. 54, p. 26–36.

Holwell, D.A., McDonald, I., and Armitage, P.E.B., 2006. Platinum-group mineral assemblages in the Platreef at the South Central pit, Sandsloot mine, northern Bushveld Complex, South Africa; Mineralogical Magazine, v. 70, p. 83–101.

Holwell, D.A., Abraham-James, T., Keays, R.R., and Boyce, A.J., 2012. The nature and genesis of marginal Cu-PGE-Au sulphide mineralization in Paleogene Macrodikes of the Kangerlussuaq region, East Greenland; Mineralium Deposita, v. 47, p. 3–21.

Hutchinson, D., White, R., Cannon, W., and Schulz, K., 1990. Keweenawan hot spot: Geophysical evidence for a 1.1 Ga mantle plume beneath the Midcontinent Rift system; Journal of Geophysical Research, v. 95, p. 10 869–10884.

Karykowski, B.T., Maier, W.D., Groshev, N.Y., Barnes, S.J., Pripachkin, P.V., McDonald, I., and Savard, D., 2018. Critical controls on the formation of contact-style PGE-Ni-Cu mineralization: Evidence from the Paleoproterozoic Monchegorsk Complex, Kola Region, Russia; Economic Geology, v. 113, p. 911–935.

Kelly, D.P. and Vaughan, D.J., 1983. Pyrrhotine-pentlandite ore textures: A mechanistic approach; Mineralogical Magazine, v. 47, p. 453–463.

Kinloch, E.D., 1982. Regional trends in the platinum-group mineralogy of the critical zone of the Bushveld Complex, South Africa; Economic Geology, v. 77, p. 1328–1347.

Kinloch, E.D. and Peyerl, W., 1990. Platinum-group minerals in various rock types of the Merensky Reef: genetic implications; Economic Geology, v. 85, p. 537–555.

Kitakaze, A., Machida, T., and Komatsu, R., 2016. Phase relations in the Fe-Ni-S system from 875 to 650°C; The Canadian Mineralogist, v. 54, p. 175–1186.

Kosyakov, V.I. and Sinyakova, E.F., 2012. Physicochemical prerequisites for the formation of primary orebody zoning at copper-nickel sulfide deposits (by the example of the systems Fe-Ni-S and Cu-Fe-S); Russian Geology and Geophysics, v. 53, p. 861–882.

Krogh, T.E., 1973. A low contamination method for hydrothermal decomposition of zircon and extraction of U and Pb for isotopic age determinations; Geochimica et Cosmochimica Acta, v. 37, p. 485–494.

Krogh, T.E., Corfu, F., Davis, D.W., Dunning, G.R., Heaman, L.M., Kamo, S.L., Machado, N., Greenough, J.D., and Nakamura, E., 1987. Precise U-Pb isotopic ages of diabase dykes and mafic to ultramafic rocks using trace amounts of baddeleyite and zircon; *in* Mafic Dyke Swarms, (ed.) H.C. Halls and W.F. Fahrig; Geological Association of Canada, Special Paper 34, p. 147–152.

Le Vaillant, M., Barnes, S.J., Mungall, J.E. and Mungall, E., 2017. Role of de-gassing of the Noril'sk nickel deposits in the Permo-Triassic mass extinction event; Proceedings of the National Academy of Sciences, v. 114, p. 2485–2490.

Lesher, C.M., 1989. Komatiite-associated nickel sulfide deposits; Reviews in Economic Geology, v. 4, p. 45–101.

Li, C., Barnes, S.-J., Makovicky, E., Rose-Hansen, J., and Makovicky, M., 1996. Partitioning of nickel, copper, iridium, rhenium, platinum, and palladium between monosulfide solid solution and sulfide liquid: effects of composition and temperature; Geochimica et Cosmochimica Acta, v. 60, p. 1231–1996.

Lightfoot, P.C., 2007. Advances in Ni-Cu-PGE sulphide deposit models and implications for exploration technologies; *in* Proceedings of Exploration 07, (ed.) B. Milkereit; Fifth Decennial International Conference on Mineral Exploration, 2007, p. 629–646.

Lightfoot, P.C. and Evans-Lamswood, D.M., 2015. Structural controls on the primary distribution of mafic–ultramafic intrusions containing Ni–Cu–Co–(PGE) sulfide mineralization in the roots of large igneous provinces; Ore Geology Reviews, v. 64, p. 354–386.

Lightfoot, P.C., Naldrett, A.J., and Hawkesworth, C.J. 1984. The geology and geochemistry of the Waterfall Gorge section of the Insizwa Complex with particular reference to the origin of the

nickel sulphide deposits; Economic Geology, v. 79, p. 1857–1879.

Liu, Y. and Brenan, J., 2015. Partitioning of platinum-group elements (PGE) and chalcogens (Se, Te, As, Sb, Bi) between monosulfide-solid solution (MSS), intermediate solid solution (ISS) and sulfide liquid at controlled fO_2-fS_2 conditions; Geochimica et Cosmochimica Acta, v. 159, p. 139–161.

Ludwig, K.R., 2003. User's manual for Isoplot 3.00: A geochronological toolkit for Microsoft Excel; Berkeley Geochronology Center, Special Publication No. 4, 71 p.

Mainwaring, P.R. and Watkinson, D.H., 1981. Origin of chromian spinel in the Crystal Lake Intrusion, Pardee Twp., Ontario; *in* Geoscience Research Grant Program, Summary of Research, (ed,) E.G. Pye; Ontario Geological Survey, Miscellaneous Paper 98, p. 180–186.

Mansur, E.T., Barnes, S.J., and Duran, C.J., 2019. Textural and compositional evidence for the formation of pentlandite via peritectic reaction: Implications for the distribution of highly siderophile elements; Geology, v. 47, p. 351–354.

Miller, J.D. and Nicholson, S.W., 2013. Geology and mineral deposits of the 1.1 Ga Midcontinent Rift in the Lake Superior region – An overview; *in* Field Guide to the Cu-Ni-PGE Deposits of the Lake Superior Region, (ed.) J.D. Miller; Precambrian Research Center Guidebook 13-1, p. 1–50.

Mungall, J.E., Andrews, D.R.A., Cabri, L.J., Sylvester, P.J., and Tubrett, M., 2005. Partitioning of Cu, Ni, Au, and platinum-group elements between monosulfide solid solution and sulfide melt under oxygen and sulfur fugacities; Geochimica et Cosmochimica Acta, v. 69, p. 4349–4360.

Mungall, J.E., Brenan, J.M., Godel, B., Barnes, S.J., and Gailard, F., 2015. Transport of S, Cu and Au in magmas by flotation of sulphide melt on vapour bubbles; Nature Geoscience, v. 8, p. 216–219.

Naldrett, A.J., 1997. Key factors in the genesis of Noril'sk, Sudbury, Jinchuan, Voisey's Bay and other world-class Ni–Cu–PGE deposits: Implications for exploration; Australian Journal of Earth Science, v. 44, p. 283–315.

Naldrett, A.J., 2004. Magmatic Sulfide Deposits: Geology, geochemistry and exploration; Springer Verlag, Heidelberg, Germany, 728 p. doi:10.1007/978-3-662-08444-1

O'Brien, S., 2018. Geology of the Crystal Lake Gabbro and the Mount Mollie Dyke, Midcontinent Rift, Northwest Ontario; M.Sc. thesis, Lakehead University, Thunder Bay, Ontario, 350 p.

Piispa, E.J., Smirnov, A.V., Pesonen, L.J., and Mitchell, R.H., 2018. Paleomagnetism and geochemistry of ~1144 Ma lamprophyre dikes, Northwestern Ontario; Implications for the North American polar wander and plate velocities; Journal of Geophysical Research, Solid Earth, v. 123, p. 6195–6214.

Piña, R., Gervilla, F., Barnes, S.-J., Ortega, L., and Lunar, R., 2012. Distribution of platinum-group and chalcophile elements in the Aguablanca Ni-Cu sulfide deposit (SW Spain): Evidence from a LA-ICP-MS study; Chemical Geology, v. 302, p. 61–75.

Prichard, H.M., Hutchinson, D., and Fisher, P.C., 2004. Petrology and crystallization history of multiphase sulfide droplets in a Mafic Dike from Uruguay: Implications for the origin of Cu-Ni-PGE sulfide deposits; Economic Geology and the Bulletin of the Society of Economic Geologists, v. 99, p. 365–376.

Queen, M., Hanes, J.A., Archibald, D.A., Farrar, E., and Heaman, L.M., 1996. $^{40}Ar/^{39}Ar$ phlogopite and U-Pb perovskite dating of lamprophyre dykes from the eastern Lake Superior region; Evidence for a 1.14 Ga magmatic precursor to Midcontinent Rift volcanism; Canadian Journal of Earth Sciences, v. 33, p. 958–965.

Ripley, E.M., 2014. Ni-Cu-PGE mineralization in the Partridge River, South Kawishiwi, and Eagle intrusions: A review of contrasting styles of sulfide-rich occurrences in the Midcontinent rift system; Economic Geology, v. 109, p. 309–324.

Robertson, J., Ripley, E.M., Barnes, S.J., and Li, C., 2015. Sulfur liberation from country rocks and incorporation in mafic magmas; Economic Geology, v. 110, p. 1111–1123.

Robertson, J.C., Barnes, S.J., and Le Vaillant, M., 2016. Dynamics of magmatic sulphide droplets during transport in silicate melts and implications for magmatic sulphide ore formation; Journal of Petrology, v. 56, p. 2445–2472.

Samalens, N., Barnes, S.J., and Sawyer, E.W., 2017. A laser ablation inductively coupled plasma mass spectrometry study of the distribution of chalcophile elements among sulfide phases in sedimentary and magmatic rocks of the Duluth Complex, Minnesota, USA; Ore Geology Reviews, v. 90, p. 352–370.

Smith, A.R. and Sutcliffe, R.H., 1987. Keweenawan intrusive rocks of the Thunder Bay area; Ontario Geological Survey, Miscellaneous Paper 137, p. 248–255.

Smith, J.W., Holwell, D.A., and McDonald, I., 2014. Precious and base metal geochemistry and mineralogy of the Grasvally Norite–Pyroxenite–Anorthosite (GNPA) member, northern Bushveld Complex, South Africa: implications for a multistage emplacement; Mineralium Deposita, v. 49, p. 667–692.

Smith, J., Bleeker, W., Liikane, D.A., Hamilton, M., Cundari, R., and Hollings, P., 2019. Characteristics of Ni-Cu-PGE sulphide mineralization within the 1.1 Ga Midcontinent Rift; *in* Targeted Geoscience Initiative: 2018 report of activities, (ed.) N. Rogers; Geological Survey of Canada, Open File 8549, p. 421–432.

Smyk, M.C. and Hollings, P., 2009. Mesoproterozoic Midcontinent Rift-related mafic intrusions near Thunder Bay: Update; *in* Summary of Field Work and Other Activities 2009, Ontario Geological Survey, Open File Report 6240, p. 11–15.

Stein, C.A., Stein, S., Elling, R., Keller, G.R., and Kley, J., 2018. Is the "Grenville Front" in the central United States really the Midcontinent Rift?; GSA Today, v. 28, p. 4–10.

Swanson-Hysell, N.L., Burgess, S.D., Maloof, A.C., and Bowring, S.A., 2014. Magmatic activity and plate motion during the latent stage of Midcontinent Rift development; Geology, v. 42, p. 475–478.

Swanson-Hysell, N.L., Ramezani, J., Fairchild, L.M., and Rose, I.R., 2019. Failed rifting and fast drifting: Midcontinent rift development, Laurentia's rapid motion and the driver of Grenvillian orogenesis; Geological Society of America Bulletin, v. 131, p. 913–940.

Thomas, B., 2015. Geochemistry, sulfur isotopes and petrography of the Cu-Ni-PGE mineralized Crystal Lake intrusion, Thunder Bay, Ontario; M.Sc. thesis, Indiana University, Indiana, 94 p.

Tomkins, A.G., 2010. Wetting facilitates late-stage segregation of precious metal-enriched sulfosalt melt in magmatic sulfide systems; Geology, v. 38, p. 951–954.

Van Schmus, W.R. and Hinze, W.J., 1985. The midcontinent rift system; Annual Review of Earth and Planetary Sciences, v. 13, p. 345–383.

von Gruenewaldt, G., Hulbert, L.J., and Naldrett, A.J., 1989. Contrasting platinum group element concentration patterns in cumulates of the Bushveld Complex; Mineralium Deposita, v. 24, p. 219–229.

Waldner, P. and Pelton, A.D., 2004. Critical thermodynamic assessment and modeling of the Fe-Ni-S system; Metallurgical and Materials Transactions B: Process Metallurgy and Materials Processing Science, v. 35, p. 897–907.

Wold, R.J. and Hinze, W.J., 1982. Geology and Tectonics of the Lake Superior Basin; Geological Society of America, Boulder, Colorado, Memoir 156, 280 p.

Yudovskaya, M., Kinnaird, J., Naldrett, A.J., Mokhov, A.V., McDonald, I., and Reinke, C., 2011. Facies variation in PGE

mineralization in the central Platreef of the Bushveld Complex, South Africa; The Canadian Mineralogist, v. 49, p. 1349–1384.

ADDITIONAL REFERENCES

Gerstenberger, H. and Haase, G., 1997. A highly effective emitter substance for mass spectrometric Pb isotope ratio determinations; Chemical Geology v. 136, p. 309–312.

Guillong, M., Hametner, K., Reusser, E., Wilson, S.A., and Günther, D., 2005. Preliminary characterisation of new glass reference materials (GSA-1G, GSC-1G, GSD-1G and GSE-1G) by laser ablation-inductively coupled plasma-mass spectrometry using 193 nm, 213 nm and 266 nm wavelengths; Geostandards and Geoanalytical Research, v. 29, p. 315–331.

Jackson, S.E., 2008. Calibration strategies for elemental analysis by LA-ICP-MS; *in* Short Course Series; Mineralogical Association of Canada, v. 40, p. 169–188.

Jaffey, A.H., Flynn, K.F., Glendenin, L.E., Bentley, W.C., and Essling, A.M., 1971. Precision measurement of half-lives and specific activities of ^{235}U and ^{238}U; Physical Review, v. 4, p. 1889–1906.

Jochum, K.P., Nohl, U., Herwig, K., Lammel, E., Stoll, B., and Hofmann, A.W., 2005. GeoReM; A new geochemical database for reference materials and isotopic standards; Geostandards Geoanalytical Research, v. 29, p. 333–338.

Lawley, C.J.M., Petts, D.C., Jackson, S.E., Zagorevski, A., Pearson, D.G., Kjarsgaard, B.A., Savard, D., and Tschihart, V., 2019. Precious metal mobility during serpentinization and breakdown of base metal sulphide; Lithos.

Lawley, C., Creaser, R., Jackson, S. E., Yang, Z., Davis, B., Perhsson, S., Dubé, B., Mercier-Langevin, P., and Vaillancourt, D., 2015. Unraveling the Western Churchill Province Paleoproterozoic gold metallotect: Constraints from Re-Os arsenopyrite and U-Pb xenotime geochronology and LA-ICP-MS arsenopyrite trace element chemistry at the BIF-hosted Meliadine Gold District, Nunavut, Canada; Economic Geology, v. 110, p. 1425–1454.

Ludwig, K.R., 2003. User's manual for Isoplot 3.00: A geochronological toolkit for Microsoft Excel; Berkeley Geochronology Center, Special Publication No. 4, 71 p.

Mattinson, J.M., 2005. Zircon U-Pb chemical abrasion ("CA-TIMS") method: combined annealing and multi-step partial dissolution analysis for improved precision and accuracy of zircon ages; Chemical Geology, v. 220, p. 47–66.

Söderlund, U. and Johansson, L., 2002. A simple way to extract baddeleyite (ZrO_2); Geochemistry, Geophysics, Geosystems, v. 3, 7 p. doi:10.1029/2001GC000212

Sylvester, P.J., Cabri, L.J., Tubrett, M.N., Peregoedova, A., McMahon, G., and Laflamme, J.H.G., 2005. Synthesis and evaluation of a fused pyrrhotite standard reference material for

APPENDIX 1

METHODS

U-Pb Geochronology

Three samples from the Crystal Lake Intrusion and one from the Mount Mollie dyke, weighing ~8–12 kg each, were prepared and analyzed at the Jack Satterly Geochronology Laboratory at the University of Toronto. The coarse pegmatoidal gabbro, troctolite, and granophyre samples were crushed and milled using standard methods (jaw crusher and Bico disk mill, respectively). A concentrate of heavy minerals was produced by re-processing the heavy mineral splits on a Wilfley table until a significantly reduced sample size of ~5–10 g was achieved. This was followed by standard mineral separation procedures using magnetic separation and methyn iodide methods. Baddeleyite and zircon crystals were recovered using a Wilfley table following the method of Söderlund and Johanssen (2002). U-Pb analysis was carried out using isotope dilution thermal ionization mass spectrometry methods (ID-TIMS). Prior to analysis, zircon crystals were thermally annealed and chemically etched (Mattinson 2005). The pre-treatment involved placing zircon grains in a muffle furnace at 900–1000°C for ~24–60 hours to repair radiation damage and anneal the crystal lattice, followed by a modified single-step partial dissolution procedure in ~0.10 ml of ~50% HF and 0.020 ml 7N HNO_3 in Teflon dissolution vessels at 200°C for between 2 and 12 hours.

Zircon and baddeleyite grains were rinsed with 8N HNO_3 at room temperature prior to dissolution. A ^{205}Pb-^{235}U spike solution was added to the Teflon dissolution capsules during sample loading. Minerals were dissolved using ~0.10 ml of concentrated HF acid and ~0.02 ml of 7N HNO_3 at 195°C for 3 to 5 days, then dried to a precipitate and re-dissolved in ~0.15 ml of 3N HCl overnight (Krogh, 1973). Uranium and Pb were isolated from zircon and baddeleyite in 50 µl anion exchange columns using HCl, deposited onto outgassed rhenium filaments with silica gel (Gerstenberger and Haase, 1997), and analyzed with a VG354 mass spectrometer using a Daly detector in pulse counting mode. Corrections to the ^{206}Pb-^{238}U ages for initial ^{230}Th disequilibrium in the zircon have been made assuming a Th/U ratio in the magma of 4.2. All common Pb was assigned to procedural Pb blank for zircon and baddeleyite. Dead time of the measuring system for Pb and U was 16 and 14 ns, respectively. The mass discrimination correction for the Daly detector was constant at 0.05% per atomic mass unit. Amplifier gains and Daly characteristics were monitored using the SRM 982 Pb standard. Thermal mass discrimination corrections are 0.10% per atomic mass unit. Decay constants are those of Jaffey et al. (1971). All age errors are given at the 95% confidence interval. Plotting and age calculations were achieved using Isoplot 3.00 (Ludwig, 2003).

Platinum Group Element Deportment

To fully characterize the precious metal-bearing mineral (PMM) assemblage within the Crystal Lake Intrusion, four mineralized composite samples from

drill core were selected from high-grade intervals (∑PGE+Au 1.3–3.3 ppm) for mineral separation and upgrading. Representative samples were collected from selected intervals from the vari-textured gabbros (<200 ppm Cr) and chrome-spinel-bearing units (>3000 ppm Cr) developed within the northern and southern limbs of the intrusion. Composite samples were crushed and milled to P80 of 75 µm (80% of material passing 75 µm) with 500 g splits of each sample wet sieved into +75 µm, 40–75 µm, 20–40 µm, 10–20 µm, and -10 µm size fractions. Heavy mineral concentrates were prepared at Advanced Mineral Technology Laboratory (AMTEL) through heavy liquid separation, magnetic separation, and panning of the non-magnetic concentrates. The pan tip of each size fraction was mounted in epoxy on a 1 inch monolayer polished block.

Polished mounts were analyzed at the Geological Survey of Canada using a Tescan Mira-3 field emission-scanning electron microscope (FE-SEM). Sections were scanned using the *Feature* function in Oxford Instruments Aztec software package. Automated scans were set at various magnifications (dependant on the size fraction) to identify high-density minerals, including precious-bearing minerals. An automated SEM-EDS analysis (0.5 s/element, normalized to 100 wt%) was performed on each identified feature. The data generated from each scan was subsequently reviewed and verified, with semi-quantitative analyses of representative grains obtained by SEM-EDS. Composite grains were reclassified and analyzed. The apparent area of each PMM was calculated from the measured two dimension equivalent-circle diameter. All data on PMM assemblages are presented in percentage of total area, which reflects more accurately the relative proportions of each PMM type. To obtain textural information about mineral associations and to characterize the PMMs in situ, a selection of polished thin sections representative of each composite sample were also studied using automated SEM-EDS analysis.

LA-ICP-MS Methodology

Quantitative elemental mapping of sulphides was carried out on selected areas of thick sections by laser ablation - inductively coupled plasma - mass spectrometry (LA-ICP-MS), at the Geological Survey of Canada. Analyses were conducted using a Photon Machines Analyte G2 excimer laser ablation system (λ = 193 nm), with a Helex II ablation cell, and an Agilent 7700x quadrupole ICP-MS.

The mapping procedure closely follows the method of Lawley et al. (2015, 2019). Elemental maps were constructed by rastering a focused laser beam across the sample surface to form a series of line scans. Laser conditions during the analytical sessions include a fluence of 4.25 J/cm^2, a repetition rate of 30 Hz, a spot size of 6–10 µm, and a scan speed of 6–10 µm/s. The spot size and scan speed were synchronized for each map such that the laser beam would advance one equivalent spot diameter in 1.0 second (i.e. 8 µm @ 8 µm/s). Prior to each ablation pass, the sample surface was cleaned by rastering the laser across the sample at a rate of 2–3 pulses every equivalent spot diameter. The cleaning step was followed by 50 s of washout, and then each analysis began with 20 s of background measurement (gas blank). The ablation aerosol was transported out of the Helex II cell using 1 L/min of helium gas, and was transported to the ICP-MS using ~ 1 m of Teflon tubing (2 mm I.D.), with no SQUID device attached. The carrier gas (He + ablation aerosol) was subsequently mixed with ~ 1 L/min of argon gas before entering the ICP-MS. To reduce the interference of the metal-argide species on the light PGEs (e.g. $^{65}Cu^{40}Ar$ on ^{105}Pd), a collision cell was used in the ICP-MS with a He flowrate of 4.0 ml/min. The instrumentation was tuned on NIST-612 to achieve >7000 cps/ppm on ^{175}Lu (in collision cell mode; 50 µm spot, ~7 J/cm^2 at 10 Hz), while minimizing the production of oxides (<0.2% for ThO/Th) and maintaining a U/Th ratio of ~1.0. Dwell times were optimized to 1–4 ms for major and minor elements and 3–8 ms for trace elements. The total duty cycle time to measure all masses on the ICP-MS (in time-resolved analysis mode) was 250 ms. Utilizing these settings, every 1.0 second of data collection, or the equivalent of one full spot diameter, included four isotopic measurements. These four isotopic measurements were then subsequently averaged to form one pixel/data point on the map.

The calibration procedures described by Jackson (2008) were followed during the mapping sessions to produce quantitative elemental maps. Standardization was achieved by calibrating the signals of unknowns (i.e. treating each pixel as a separate analysis) against analyses of GSE-1G (Guillong et al., 2005; for most major and trace elements) and synthetic pyrrhotite standard Po726 (Sylvester et al., 2005; for the calibration of sulphur and PGEs), and normalizing the total element, or element oxide, concentrations to 100%. Reference materials were analyzed every 20 unknowns to account for instrumental drift during the mapping session. A secondary standard, NIST-610, was analyzed every 20 unknowns and routinely yielded calculated concentrations within 15% of the accepted values for most elements. In addition, the major element compositions of all sulphide phases were routinely within 10 and 15% of the stoichiometric values (based on end-member sulphide phases). Reference values for standards GSE-1G and NIST-610 are taken from the online geological and environmental reference materials database (GeoReM; Jochum et al., 2005).

All data processing was performed using the in-house software *LAMTrace* and *PixeLAte*, and maps were constructed using an in-house *Python* script that converted concentration profiles into 2-D images. The elemental concentration maps are displayed using logarithmic and percentile colour scaling, with red colours representing the highest concentrations.

APPENDIX 2

Table A2.1. Summary of U-Pb CA-ID-TIMS isotopic data for zircon and baddeleyite from the Crystal Lake Intrusion and Mount Mollie dyke.

Sample/ Number	Fraction	U (ppm)	Th/U	Pbtot (pg)	Pbc (pg)	$^{206}Pb/^{204}Pb$	$^{207}Pb/^{235}U$	2σ	$^{206}Pb/^{238}U$	2σ	Error Corr.	$^{207}Pb/^{206}Pb$	2σ	Age (Ma) $^{206}Pb/^{238}U$	2σ	Age (Ma) $^{207}Pb/^{235}U$	2σ	Age (Ma) $^{207}Pb/^{206}Pb$	2σ	% Disc
18-SYB-001 - Unmineralized, homogeneous troctolite, northern limb; 305453.19 E, 5328330.35 N (Zone 16), 21–35 m																				
MH19055	Z1	253	1.478	61.02	0.32	9371	1.92656	0.00493	0.184297	0.000374	0.8782	0.075816	0.000094	1090.4	2.0	1090.3	1.7	1090.2	2.5	0.0
MH19056	Z2	484	1.533	118.23	0.26	21670	1.92812	0.00448	0.184288	0.000344	0.9366	0.075881	0.000066	1090.4	1.9	1090.9	1.6	1091.9	1.7	0.2
18-SYB-002 - Mineralized, vari-textured gabbro, northern limb; 305453.19 E, 5328330.35 N (Zone 16), 412–417 m																				
MH19057	Z1	615	1.315	144.02	0.18	39903	1.93414	0.00435	0.184712	0.000337	0.9324	0.075944	0.000065	1092.7	1.8	1093.0	1.5	1093.6	1.7	0.1
MH19058	Z2	329	1.315	76.90	0.35	11084	1.93207	0.00467	0.184627	0.000349	0.8977	0.075897	0.000084	1092.2	1.9	1092.3	1.6	1092.4	2.2	0.0
MH19113	Bd1	900	0.060	78.21	0.97	5510	1.93618	0.00528	0.184864	0.000336	0.8230	0.075961	0.000122	1093.5	1.8	1093.7	1.8	1094.1	3.2	0.1
MH19114	Bd2	949	0.056	128.59	2.24	3936	1.93009	0.00604	0.184414	0.000346	0.7524	0.075907	0.000161	1091.0	1.9	1091.6	2.1	1092.6	4.2	0.2
18-SYB-111 - Mineralized, vari-textured gabbro, southern limb; 306239.91 E, 5326523.72 N (Zone 16), 556–562 m																				
MH19059	Z1	567	0.792	118.32	0.21	32323	1.93275	0.00446	0.184406	0.000368	0.8851	0.076015	0.000082	1091.0	2.0	1092.5	1.5	1095.5	2.2	0.4
MH19060	Z2	414	1.243	95.22	0.20	24648	1.93047	0.00468	0.184396	0.000371	0.9404	0.075929	0.000066	1090.9	2.0	1091.7	1.6	1093.2	1.7	0.2
18-SYB-149 - Coarse granophyre, Mount Mollie dyke; 313981.01 E, 5325871.74 N (Zone 16)																				
MH19064a	Z1	185	0.218	10.06	0.42	1595	1.92532	0.01173	0.184233	0.000525	0.6097	0.075794	0.000372	1090.1	2.9	1089.9	4.1	1089.6	9.8	0.0
MH19065a	Z2	241	0.217	13.10	3.07	297	1.93971	0.05663	0.184207	0.000666	0.7775	0.076371	0.002025	1089.9	3.6	1094.9	19.7	1104.8	53.4	1.5
MH19066a	Bd1	1006	0.019	463.44	9.59	3352	1.93041	0.00654	0.184122	0.000356	0.7029	0.076040	0.000186	1089.5	1.9	1091.7	2.3	1096.1	4.9	0.7
MH19109	Bd2	1092	0.034	603.24	3.68	11264	1.91003	0.00468	0.182245	0.000351	0.8995	0.076012	0.000084	1079.2	1.9	1084.6	1.6	1095.4	2.2	1.6
MH19110	Bd3	632	0.016	358.96	3.10	8000	1.92584	0.00491	0.183508	0.000349	0.8805	0.076114	0.000096	1086.1	1.9	1090.1	1.7	1098.1	2.5	1.2
MH19111	Bd4	806	0.026	151.12	4.80	2184	1.92239	0.00861	0.183335	0.000361	0.6339	0.076049	0.000272	1085.2	2.0	1088.9	3.0	1096.4	7.2	1.1
MH19112	Bd5	883	0.014	229.51	3.75	4245	1.92467	0.00600	0.183615	0.000387	0.7467	0.076023	0.000159	1086.7	2.1	1089.7	2.1	1095.7	4.2	0.9

Notes:
All zircon grains have been thermally annealed and etched in HF (Mattinson, 2005).
Z = zircon; Bd = baddeleyite.
Th/U calculated from radiogenic $^{208}Pb/^{206}Pb$ ratio and $^{207}Pb/^{206}Pb$ age, assuming concordance.
Pbc is total common Pb, assuming the isotopic composition of laboratory blank ($^{206}Pb/^{204}Pb$=18.49±0.4%; $^{207}Pb/^{204}Pb$=15.59±0.4%; $^{208}Pb/^{204}Pb$=39.36±0.4%).
$^{206}Pb/^{204}Pb$ corrected for fractionation and common Pb in the spike.
Pb/U ratios corrected for fractionation, common Pb in the spike, and blank.
Correction for ^{230}Th disequilibrium in $^{206}Pb/^{238}U$ and $^{207}Pb/^{206}Pb$ assuming a Th/U of 4.2 in the magma.
% Disc. is percent discordance for the given $^{207}Pb/^{206}Pb$ age.
Error Corr. is the correlation coefficient for X-Y errors in the concordia plot.
Decay constants are those of Jaffey et al. (1971): ^{238}U = 1.55125 x 10^{-10}/yr, ^{235}U = 9.8485 x 10^{-10}/yr.